nologies, Inc.
 Lane, #330
80201

TORING AGENCY NAME(S) AND ADDRESS(ES)   10.

:search Office
11
ngle Park, NC 27709-2211

A

COHERENT TECHNOLOGIES, INC.

P.O. Box 7488 Boulder, Colorado 80306-7488

REPORT DOCUMENTATION PAGE

Form Approved
OMB No. 0704-0188

Public reporting burden for this collection of information is estimated to average 1 hour per response, including the time for reviewing instructions, searching existing data sources, gathering and maintaining the data needed, and completing and reviewing the collection of information. Send comments regarding this burden estimate or any other aspect of this collection of information, including suggestions for reducing this burden, to Washington Headquarters Services, Directorate for Information Operations and Reports, 1215 Jefferson Davis Highway, Suite 1204, Arlington, VA 22202-4302, and to the Office of Management and Budget, Paperwork Reduction Project (0704-0188), Washington, DC 20503.

1. AGENCY USE ONLY (Leave blank)	2. REPORT DATE	3. REPORT TYPE AND DATES COVERED
	July 1992	Final 1 Feb 92 - 31 Jul 92

4. TITLE AND SUBTITLE
Coherent Lidar System for High Resolution Measurement
of Atmospheric Wind Velocity and Water Vapor Fields

5. FUNDING NUMBERS
DAAL03-92-C-0004

6. AUTHOR(S)
J. Alex Thomson, Stephen M. Hannon,
Paul J.M. Suni, R. Milton Huffaker

7. PERFORMING ORGANIZATION NAME(S) AND ADDRESS(ES)
Coherent Technologies, Inc.
3300 Mitchell Lane, #330
Boulder, CO 80201

8. PERFORMING ORGANIZATION REPORT NUMBER

9. SPONSORING/MONITORING AGENCY NAME(S) AND ADDRESS(ES)
U. S. Army Research Office
P. O. Box 12211
Research Triangle Park, NC 27709-2211

10. SPONSORING/MONITORING AGENCY REPORT NUMBER
ARO 29496.1-GS-SBI

11. SUPPLEMENTARY NOTES
The view, opinions and/or findings contained in this report are those of the author(s) and should not be construed as an official Department of the Army position, policy, or decision, unless so designated by other documentation.

12a. DISTRIBUTION/AVAILABILITY STATEMENT

Approved for public release; distribution unlimited.

12b. DISTRIBUTION CODE

13. ABSTRACT *(Maximum 200 words)*

The objective of this study is to evaluate the capability for a scanning coherent pulsed laser to acquire high resolution, time dependent mapping of the three dimensional structure of wind velocity and water vapor in the turbulent planetary boundary layer. Power, pulse length, prf, and sampling requirements have been established that will permit achievement of 25 to 50 meter 3D spatial resolution with better than 1 meter/second velocity resolution throughout a 3 cubic kilometer volume of boundary layer in a 5 second update time using near term 1 or 2 micron laser systems. Signal processing techniques are outlined (and demonstrated with simulations) that can merge line-of-signt wind component measurements from a single station laser radar with multi-dimensional Boundary layer dynamic models to retrieve the full vector wind field. Simultaneous DIAL measurements (at 2 microns laser wavelength) can be used to measure large scale water vapor fluctuations. A correlation technique to infer small scale water vapor fluctuations fields from observations of the more readily detected fluctuations of backscatter intensity is proposed. Data taken with two available scanning lidars (1 and 2 microns wavelength) is presented to demonstrate the spatial resolutions achievable. A program for implementing a full 3D demonstration measurement is outlined.

14. SUBJECT TERMS
Doppler laser radar, atmospheric boundary layer, turbulence, water vapor, DIAL, Kalman filter, correlation.

15. NUMBER OF PAGES
62

16. PRICE CODE

17. SECURITY CLASSIFICATION OF REPORT	18. SECURITY CLASSIFICATION OF THIS PAGE	19. SECURITY CLASSIFICATION OF ABSTRACT	20. LIMITATION OF ABSTRACT
UNCLASSIFIED	UNCLASSIFIED	UNCLASSIFIED	UL

NSN 7540-01-280-5500

Standard Form 298 (Rev 2-89)
Prescribed by ANSI Std Z39-18

2

TECHNICAL REPORT CTI-TR-9206

COHERENT LIDAR SYSTEM FOR HIGH
RESOLUTION MEASUREMENT OF
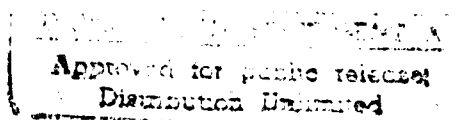ATMOSPHERIC WIND VELOCITY AND
WATER VAPOR FIELDS

July 1992

ARO Contract Number DAAL03-92-C-0004

J. Alex Thomson
Stephen M. Hannon
Paul J. M. Suni
R. Milton Huffaker

Coherent Technologies, Inc.
3300 Mitchell Lane, Suite 330
Boulder, CO 80301 USA
(303) 449-8736

U.S. Army Research Office
P.O.Box 12211
Research Triangle Park, NC 27709-2211

THE VIEW, OPINIONS, AND/OR FINDINGS CONTAINED IN THIS REPORT ARE THOSE OF THE AUTHOR(S) AND SHOULD NOT BE CONSTRUED AS AN OFFICIAL DEPARTMENT OF THE ARMY POSITION, POLICY, OR DECISION, UNLESS SO DESIGNATED BY OTHER DOCUMENTATION.

ACKNOWLEDGMENTS

Accession For		
NTIS CRA&I		X
DTIC TAB		☐
Unannounced		☐
Justification		
By		
Distribution /		
Availability Codes		
Dist	Avail and / or Special	
A-1		

TABLE OF CONTENTS

FIGURES AND TABLES

Coherent Lidar System for High Resolution Measurement of Atmospheric Wind Velocity and Water Vapor Fields

I. SUMMARY

1.1 OVERVIEW

The goal of this study is to evaluate the capability for a scanning coherent pulsed laser radar/lidar, to achieve a high resolution mapping of the three dimensional structure of wind velocity and water vapor in the turbulent planetary boundary layer. This information is needed to validate models of turbulent dispersion in the atmospheric boundary layer under a variety of stability and terrain conditions. It is generally recognized that intermittent or sporadic coherent events in the boundary layer may play a vital part in determining the overall transport mechanisms, both of species as well as momentum and energy. Large scale 3D computations of boundary layer dynamics are playing an increasing role in the development of the understanding of these transport processes. It is of particular interest to obtain quantitative observations of the eddy transport mechanics at the grid scales of these computations (several tens of meters) so that comparisons can be made and models of the transport can be validated.

Since its inception in 1984 Coherent Technologies, Inc. (CTI) has been developing scanning solid-state coherent lidars that have the ability to probe the atmospheric boundary layer at scales relevant to the description of atmospheric boundary layer wind fields. The basic objective of the present study is to determine the feasibility and to construct a conceptual design of a lidar system for measuring both the turbulence itself (wind velocity fluctuations) and its consequence (transport) to meet the above objectives. For this purpose the study has been divided into four tasks:

1. Generate realistic examples of wind velocity and water vapor turbulent or fluctuation fields and simulate the properties of a scanning lidar diagnostic system to make Doppler measurement of line-of-sight velocity and DIAL (Differential Absorption Lidar) measurements of water vapor concentration.

2. Predict performance and measurement precisions to be expected for line of sight velocity and concentrations as a function of space and time resolution, scan coverage, atmospheric environment, and lidar parameters.

3. Demonstrate velocity measurement capability in the boundary layer and validate basic parameters of the prediction models and measurement concepts using available Doppler lidar scanning systems.

4. Construct a conceptual design of a prototype system for turbulence measurements in the planetary boundary layer.

There are basically three lidar measurement and data analysis concepts that can be considered for measuring properties of the turbulent atmospheric boundary layer. In order of increasing complexity these are:

1. Conventional sampling at one or more space points from one or more view directions of the time history of the local radial (line-of-sight) wind followed by a multidimensional spectral or conditional sampling analysis to construct the statistical properties of the local wind field.

2. Measurement of the spatial distribution of the radial wind component over a 3 dimensional measurement field followed by a data analysis that imposes continuity, persistence, spatial uniformity or other constraints to restrict the form of allowed solutions and to fit these forms to the data.

3. Incorporation of the radial wind components measured by the lidar as a function of space and time into a full-blown 3D hydrodynamic calculation of the boundary layer flow.

A major result of the present study is the conclusion that lidar and signal processing capabilities that have recently become available allow realistic implementation of the third concept. The first two concepts have been extensively used in the past, require limited sampling of the flow environment, and can be implemented with limited scanning and signal processing tools. The third requires a full 3D scanning capability together with a signal processing that can retrieve the 3D distribution of the vector wind field. The second method, which includes such concepts as VAD and cloud tracking, is essentially a derivative of the third with idealized assumptions introduced to limit the measurement and processing requirements (such as horizontally homogeneous winds and/or 'frozen' turbulence). The first method is a statistical treatment of the wind field measurements designed to extract stationary measures of the flow and can be applied directly to the measurements in real time or to recorded data. Given that the third method is possible it provides data that can be processed after the measurement using such statistical techniques.

This report will emphasize the third approach. To retrieve both vector winds and water vapor concentration at small turbulence scales, we have found it necessary to develop two new signal processing concepts. First, a processing concept has been developed to retrieve three component vector winds from the one component line-of-sight velocity measurements by the imposition of known hydrodynamic constraints (mass conservation and momentum conservation). This procedure is basically an extension of a well-known method used to retrieve vector winds from two station radar data (Dual Doppler method).[1] For application to lidar we have extended this method to apply to single station data by structuring the signal processing analysis in a Bayesian estimation framework that merges the measurements with a complete description of the equations governing the boundary layer dynamics.

---

[1]R.J. Doviak and D.S. Zrnic, "Doppler Radar and Weather Observations," Chapt. 9, Academic Press (1984)

A second measurement and processing concept has been developed to allow Doppler velocity data and DIAL measurements of water vapor concentration to be combined and interpreted in terms of small scale correlations and transport. The major problem with DIAL for turbulence studies is its limited capability for sensing small scale structures. DIAL is an indirect method for sensing species concentrations that relies on spatial and spectral differencing to interpret absorption features of the reflected light in terms of local species concentrations. This differencing at small spatial scales represents a major source of noise at the weak reflection levels characteristic of atmosphere aerosol backscatter and effectively precludes the making of accurate measurements at turbulence scales. The technique proposed here utililizes DIAL to establish a correlation at large scales between water vapor density fluctuations and fluctuations of the backscattering coefficient due to aerosols. Both are passively advected by the turbulent wind field and similar correlation is to be expected at both large and small scales. Since the fluctuations of aerosol density are much more easily measured at small scales than are the absorption fluctuations, an effective method of extending DIAL to small scales is to measure both absorption (using DIAL) and backscatter at large scales, establish a correlation coefficient, and use the correlation coefficient to infer small scale water vapor fluctuations from similar fluctuations in the measured backscatter.

Evaluation of the expected performance and simulation of the data processing have been carried out to validate the concepts and determine the system measurement capability. The results of the analyses are described in the following section.

1.2 RESULTS SUMMARY

1.2.1 VELOCITY ERROR EXPECTATIONS

At high SNR the precision with which the velocity can be estimated in a single pulse is determined by the width of the Doppler spectrum. For short pulses the width is determined by the pulse duration. For long pulses the spectrum represents the spread of aerosol velocities within the pulse. Figure 1.1 shows the dependence of this width on the subgrid turbulence level and lidar wavelength. For a pulsed system in the absence of turbulence, the product of expected velocity error standard deviation (per pulse) and pulse length is a constant.

For atmospheric turbulence measurements we have assumed that a velocity precision of the order of 1.0 meter/second or better per pulse is adequate to monitor the turbulence when many pulses sample the 3D observational volume. Greater velocity precision can be achieved by averaging pulses at the expense of decreased spatial resolution or coverage. Figure 1.1 shows that this requirement limits the achievable spatial range resolution to about 50 meters at 2 microns wavelength. For a given velocity precision, the spatial resolution is proportional to wavelength in the absence of sub grid turbulence (i.e., 250 meters at 10 microns and 25 meters at 1 micron). In general, shorter wavelengths are preferred for a pulsed system when both high velocity and spatial resolution are required. In numerical simulations of the velocity retrieval we
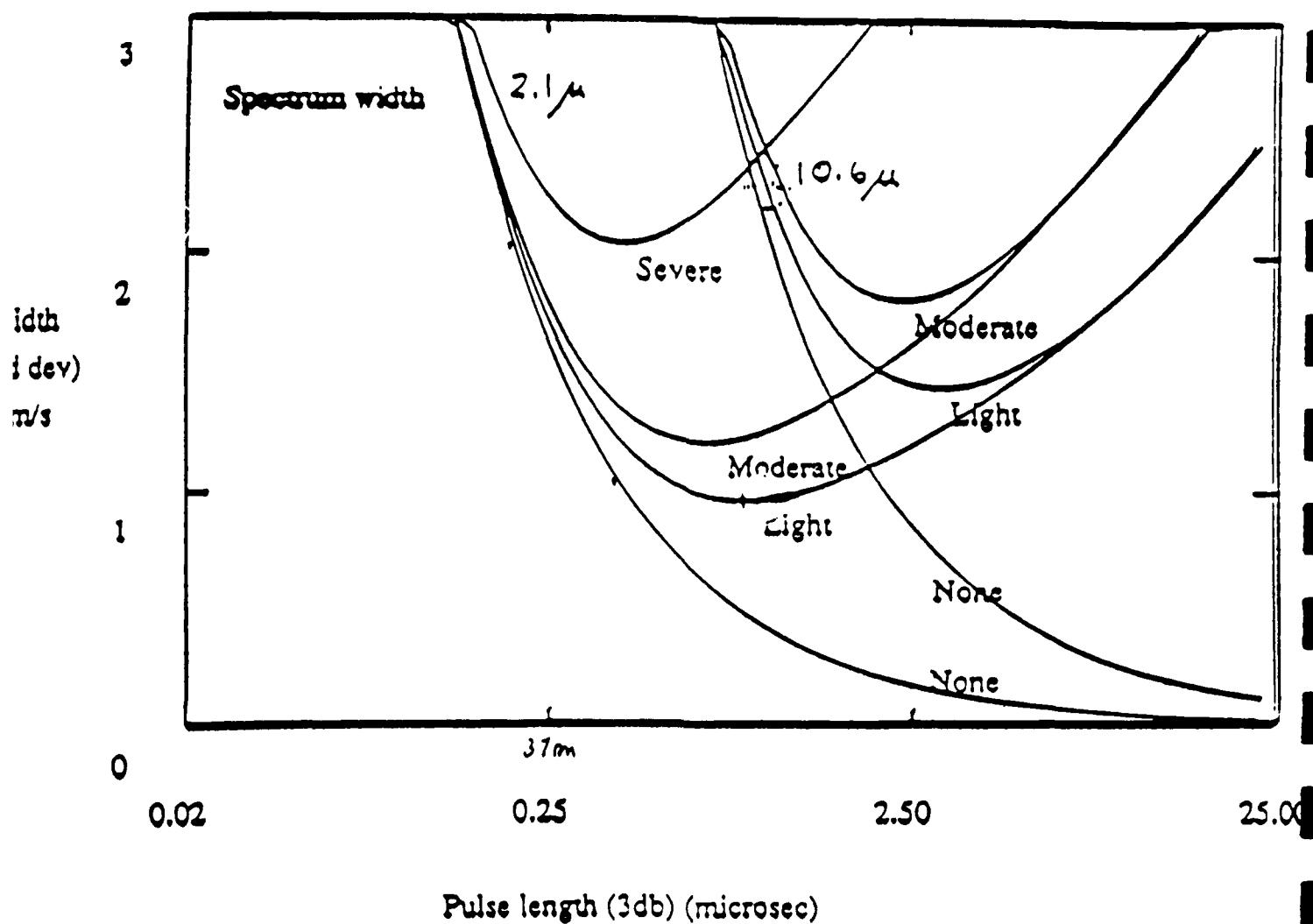
Figure 1.1 Spectrum width. The Doppler spectrum width can be minimized in the presence of turbulence by appropiate choice of pulse length. Smaller widths can be achieved at smaller wavelengths.

have found that maintaining a high lateral resolution also assists in maintaining a high range resolution as a result of the coupling to the fluid dynamic constraints of the flow.

In the presence of turbulence, the expected velocity error shows a minimum as a function of pulse length at the point where the spectral broadening due to the finite pulse length is comparable to that created by the spread of aerosol radial velocities within the pulse. For light to moderate turbulence this occurs at a pulse length of order 100 meters at 2 microns. The achievable velocity resolution is then relatively insensitive to pulse lengths over the range 50 to 150 meters.

In general we expect that achievable spatial resolution in the direction of look for a pulsed coherent Doppler lidar designed to probe atmospheric turbulence will be limited to about 25 to 50 meters at 1 and 2 microns respectively. Some benefit may result from high density angular sampling and/or shorter pulses with multiple pulse averaging. On the basis of these considerations we have assumed a nominal design requirement of 25 to 50 meters lateral separation of the lines of sight. This will lead to the specification of at least 300 Hz prf with at least 1 watt mean power to probe a volume 1 km x 1 km in lateral extent and 1 to 3 km long with a 3 second update period. Both a one micron and a two micron system are candidates. At ten microns focusing with long or CW pulses is needed to achieve adequate range resolution. This will severely limit the maximum allowable range. In general one micron has best resolution under ideal conditions but is not eyesafe and is more readily degraded by refractive turbulence.

1.2.2. SIMULATIONS

Several simulation models are available at CTI to characterize the lidar reponse to both localized wind and aerosol patterns. These models provide estimates of the measurement precision expected as a function of lidar system design and atmospheric state. Simulations of candidate turbulence wind fields have been generated in two dimensions and have been used in a simulation of the measurement concept. In these simulations a two dimensional Kalman filter accepts radial velocity measures made at arbitrary space and time coordinates in a vertical plane and incorporates these into a numerical 2D incompressible hydro model of the boundary layer. The 2D code is not appropriate for the real atmospheric boundary layer but is being used to test the data assimilation procedures. A full 3D code will be required for the actual assimilation and nowcasting of real data. In the 2D analysis each line of sight is intended to represent a plane of 3D data.

Figures 1.2 and 1.3 show examples of the operation and type of output of this analysis. Measurements of the radial wind are assumed to be continuously collected along several lines of sight. In the simulation these wind fields were generated by a 2D hydrodynamic boundary layer code. These simulated measurements are fed to a Kalman filter which continuously updates a similar 2D hydro code describing the vector wind field in a vertical plane containing the measurement points. The difference between the measured data and the code predicted data at the measurement points forms a source of distributed vorticity throughout the computational volume that allows
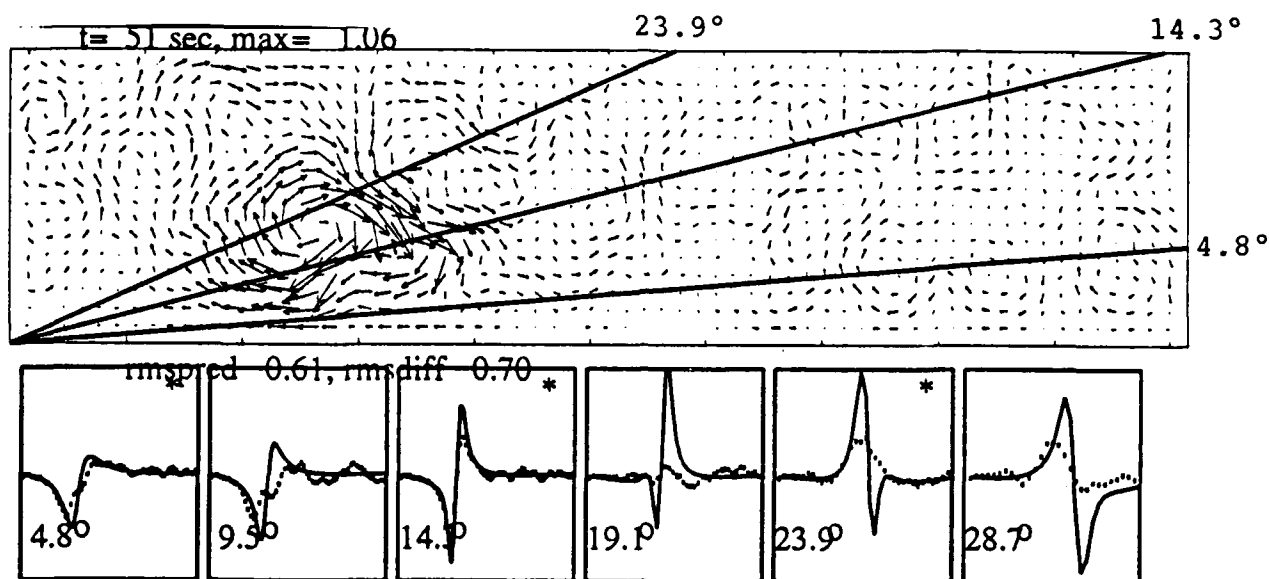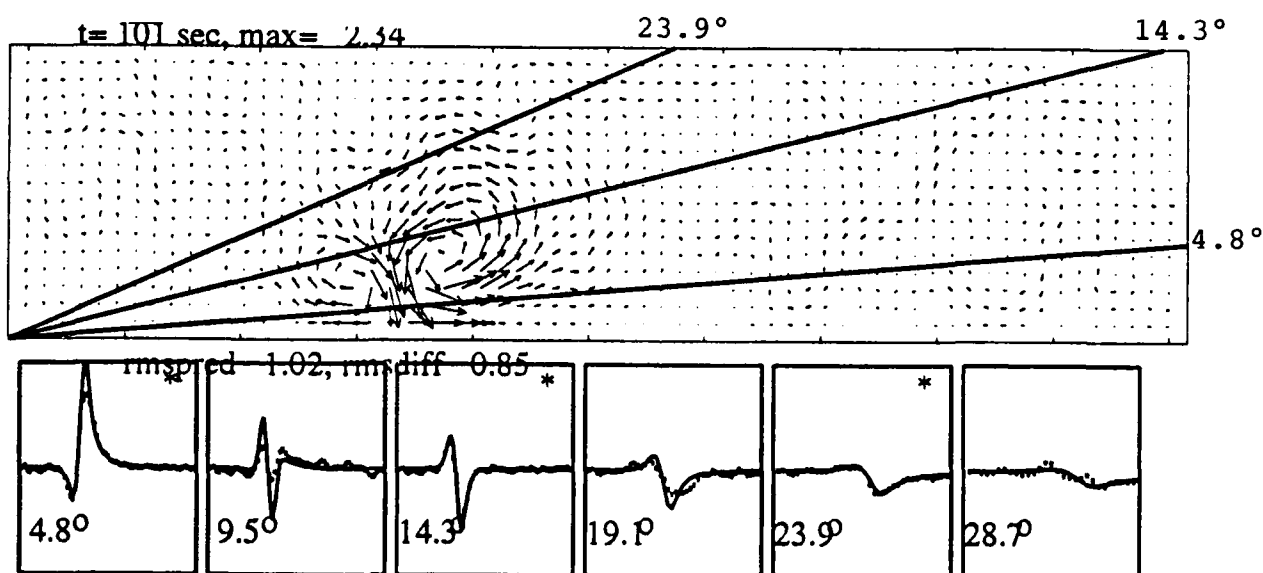
Figure 1.2. Kalman filter simulation to adapt a 2D boundary layer hydro code to
simulated lidar measurements of the near surface line-of-sight winds.
(a) Velocity patterns and line-of-sight velocity components at 51 seconds.
The lower panels compare the simulated measurements(solid line) with
the current estimate (dots) provided by the nowcast output of the hydro
code. Panels marked with an asterisk identify participating lines of sight.
(b) Evolution of the estimated 2D field at 101 seconds. At this time the
predicted data are in essential agreement with the measured data.
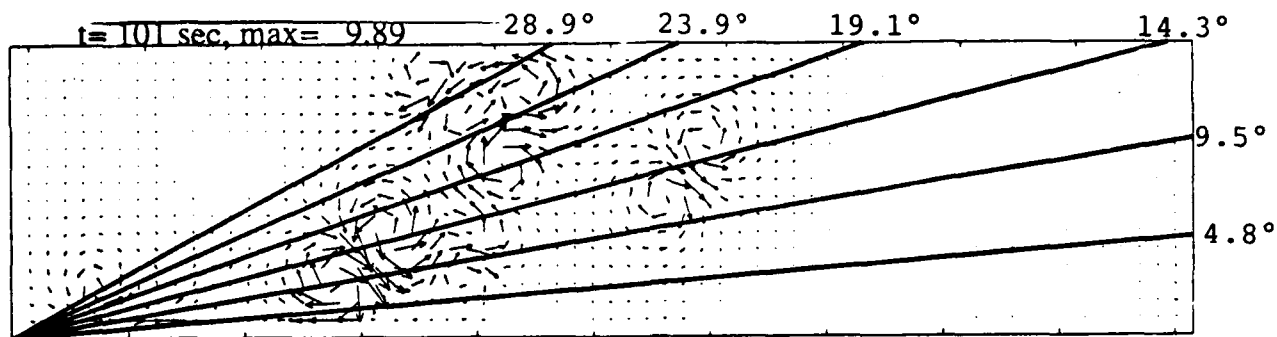
(a)

(b)
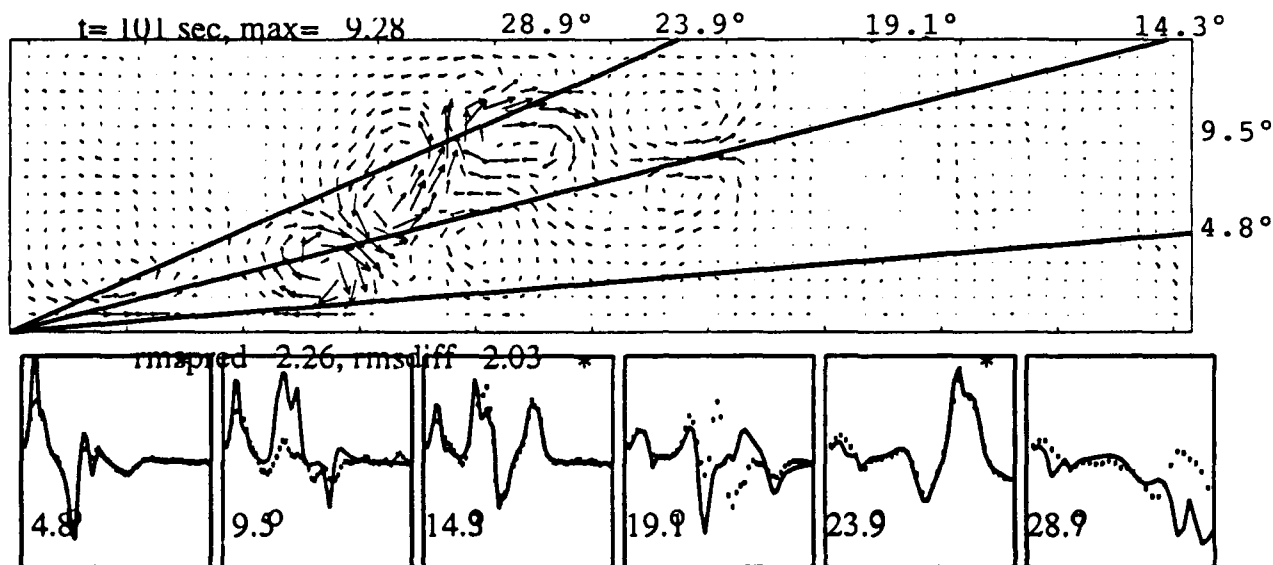

(c)
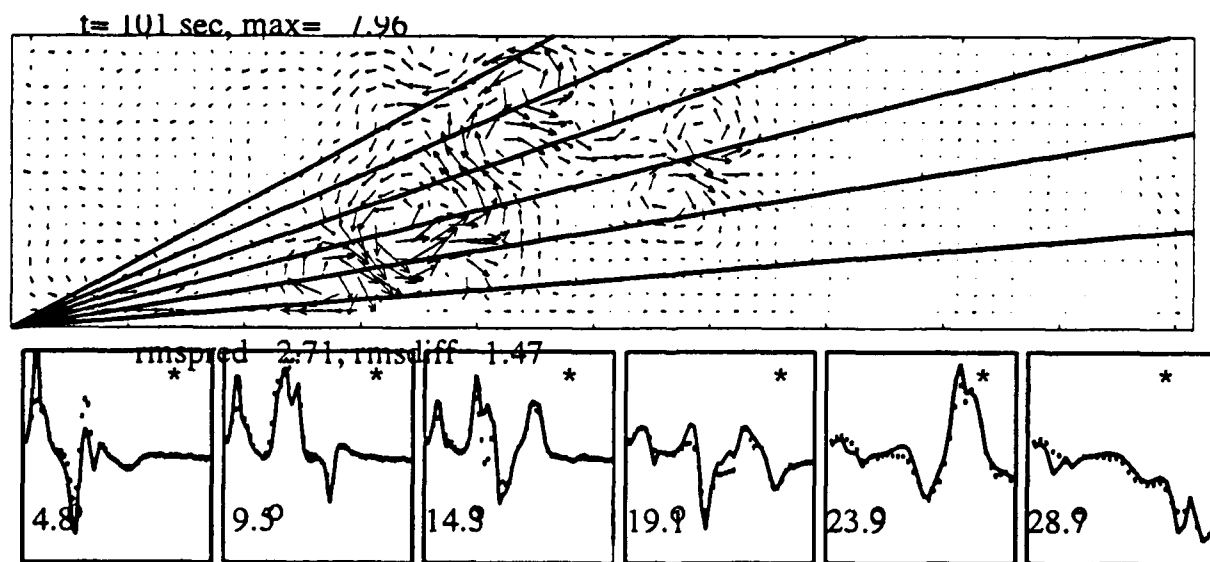
Figure 1.3. Kalman filter simulation to adapt a 2D boundary layer hydro code to simulated lidar measurements of line-of-sight winds.
(a) True velocity patterns at time 101 seconds
(b) Velocity patterns and line-of-sight velocity components inferred from three lines of sight.
(c) Velocity patterns and line-of-sight velocity components inferred from six lines of sight.

8

the atmosphere to adapt to the measurements. The algorithms and implementation of this procedure is described in detail in the Section 3.1.

Figure 1.2 shows the adaption to a wind field created by a simple vortex pair representation of a wind gust. Simulated data has been acquired along three lines of sight. In the reconstruction, the inferred atmosphere is assumed to be initially motionless at time 0. The Kalman filter then generates and advects vorticity to allow the atmosphere to adapt to the measurements. In this example the vector velocity field becomes well reconstructed throughout the region displayed within 100 seconds after initation of the adaptation.

Reconstructions of a more complex wind field are shown in Figure 1.3. The true velocity field at time 100 seconds is shown in panel a and reconstructions using 3 and 6 lines of sight in panels b and c. In this case the reconstruction with 3 lines of sight is less satisfactory than in the prior example even though the deduced field at the measurement points is very accurate. With 6 lines of sight the inferred field is well predicted throughout the measurement field.

As is apparent from these examples the inferred field is one possible solution, but not the only one. When only a small number of lines of sight are measured, there are potentially many possible atmospheric flows that can reproduce the measurements. As demonstrated in Figure 1.3 fine gridding of the lines of sight can reduce the level of ambiguity and improve the quality of the inferred field.

These calculations demonstrate that a hydrodynamically constrained analysis can be used to generate vector winds from measurements of only one component.

1.3 WATER VAPOR MEASUREMENT USING DIAL

DIAL meaurements of the type discussed in Section 1.1 require a high prf source (typically 300 Hz) that can be switched between an absorbing (A) and non-absorbing (N) wavelength. In selecting suitable wavelengths for DIAL measurements, several issues must be considered. First, the non-absorbing one should have quite a low attenuation over the desired range. Second, the absorbing one should have an attenuation that is not too weak, but also not too strong. If it is weak, the differential absorption becomes more difficult, while if it is too strong, there may not be enough signal to make an accurate estimate of water vapor from the furthest range. The A wavelength must also be directly associated with water absorption, and should ideally not be contaminated by absorption due to other species.

Figure 1.4a shows the MLS (Mid-latitude Summer) attenuation spectrum in the region of tuning of Tm:YAG lasers. There is a clear CO_2 overtone band covering much of the region, as well as other peaks associated with water and NO_2. Figure 1.4b shows the water spectrum alone. Several of the water lines overlap directly with CO_2 lines and are therefore unsuitable for the present application. The line marked with an arrow and the letter A at 2016.974 nm (vacuum wavelength) has a peak extinction coefficient of 3.389 (per km roundtrip) and is virtually free from contamination by neighboring CO_2
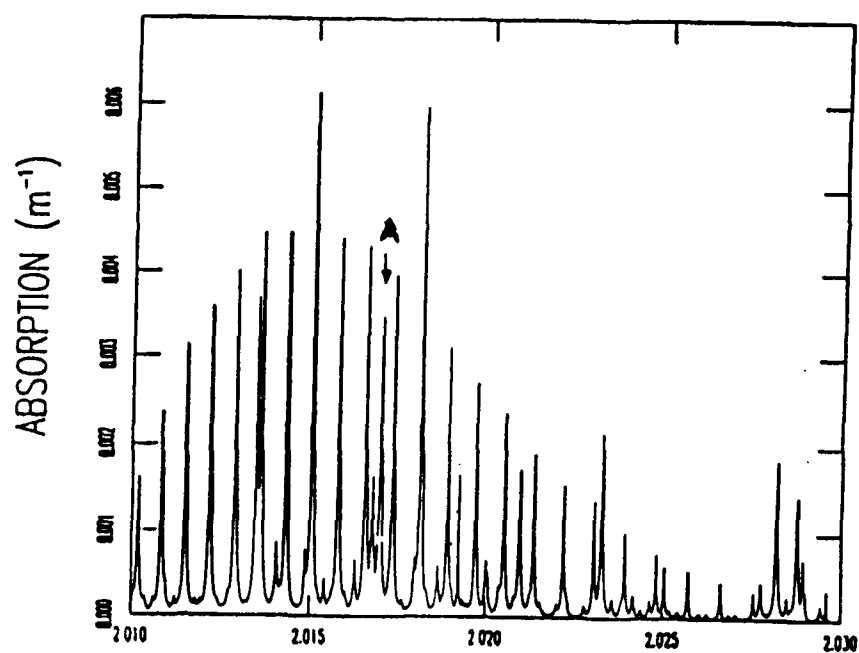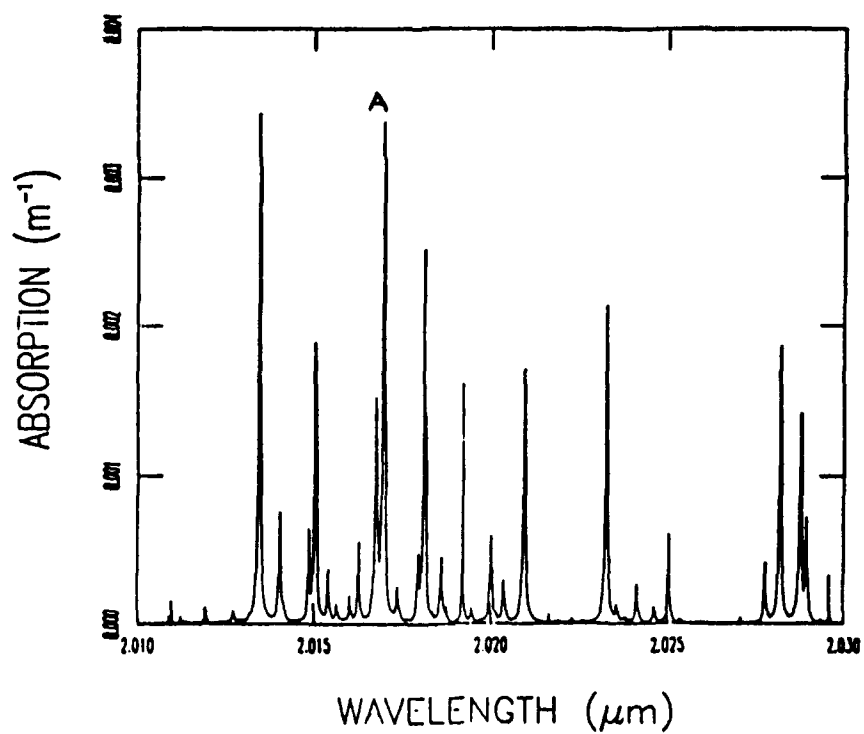
Figure 1.4 Absorption coefficients at sea level for a mid latitude summer
atmosphere (a). Contribution of water vapor only (b).

lines (these lines contribute < 3% of the total attenuation. It is therefore an excellent choice for short-range water vapor measurements.

For the non-absorbing wavelength, the best choice is to operate at 2017.713 nm. The valley shows a total absorption of 0.1 per km at that point (0.4 db per km roundtrip). The width of the valley floor is approximately 0.078 nm, corresponding to 5.8 GHz.

Both of these wavelengths are easily accessible with an injection-seeded Tm:YAG laser. Continuous tuning from 2006 to 2023 nm has been demonstrated at CTI.

1.4 CANDIDATE MEASUREMENT AND PROCESSING CONCEPTS

The ultimate lidar boundary layer sensor would have the ability to probe a three dimensional volume and produce a detailed map of the line of sight velocity field with of order 20 meter resolution throughout a 1 kilometer cube of atmosphere at a refresh rate of 0.2 to 0.5 Hz. Such a direct data sensing system would operate at up to a kilohertz pulse repetition frequency, and would require up to 10 watts mean power, and would require multiple ground installations to retrieve the full vector field.

The basic premise of the current analysis is that a much less capable system in terms of hardware can be expected to perform the same basic interrogation task if combined with suitable data processing. The required data processing must recognize that the 'normal' atmosphere dynamics are severely limited by requirements of continuity and momentum conservation. Appropriate merging of these constraints with the measured data can substantially lessen the sensing requirements without materially restricting the validity of the intepretation of the observation. The goal of the present study is to define and test examples of such combined measurement and data analysis concepts using available scanning lidar systems.

We envisage monitoring the radial wind over multiple vertical or horizontal planes, each 1.5 km wide by 3 km long, centered at a horizontal range of 3 or 4 km. With a mesh spacing equal to the pulse length (50 meters) the advection time across the mesh cell at a mean wind speed of 10 meters/sec is 5 seconds. Thus, we will need an update rate of something like 0.2 Hz to follow advecting wind patterns. This coverage will require about 30 pulses per plane every 5 seconds (a prf of 6 pulses per plane per second) and would allow a lateral coverage of a 1.5 km and a longtitudinal coverage of at least 3 km. Thus we envisage monitoring the radial wind over multiple vertical or horizontal planes, each 1.5 km wide by 3 km long centered at a horizontal range of 3 or 4 km. With a mean wind speed of 10 meters per second this allows at total observation time will be 2 to 5 minutes before the scene would entirely decorrelate (total of 750 to 1500 pulses transmitted per plane and available for data analysis - a net density of 30 range gates per plane, spread out in time, per horizontal resolution cell).

The issue is how many measurement planes will be required. Figures 1.5 shows the expected measurement characteristics for a candidate measurement that uses relatively dense sampling (40 planes). Here a 2 km x 2 km x 2 km cube centered at 3 km horizontal range is to be scanned by a single ground lidar. The lidar is assumed to operate at 2 watts mean power, with a 320 pulse per sec repetition frequency, and with a pulse length of 0.3 microseconds (FWHM). At a refresh rate of 0.2 Hz this provides a
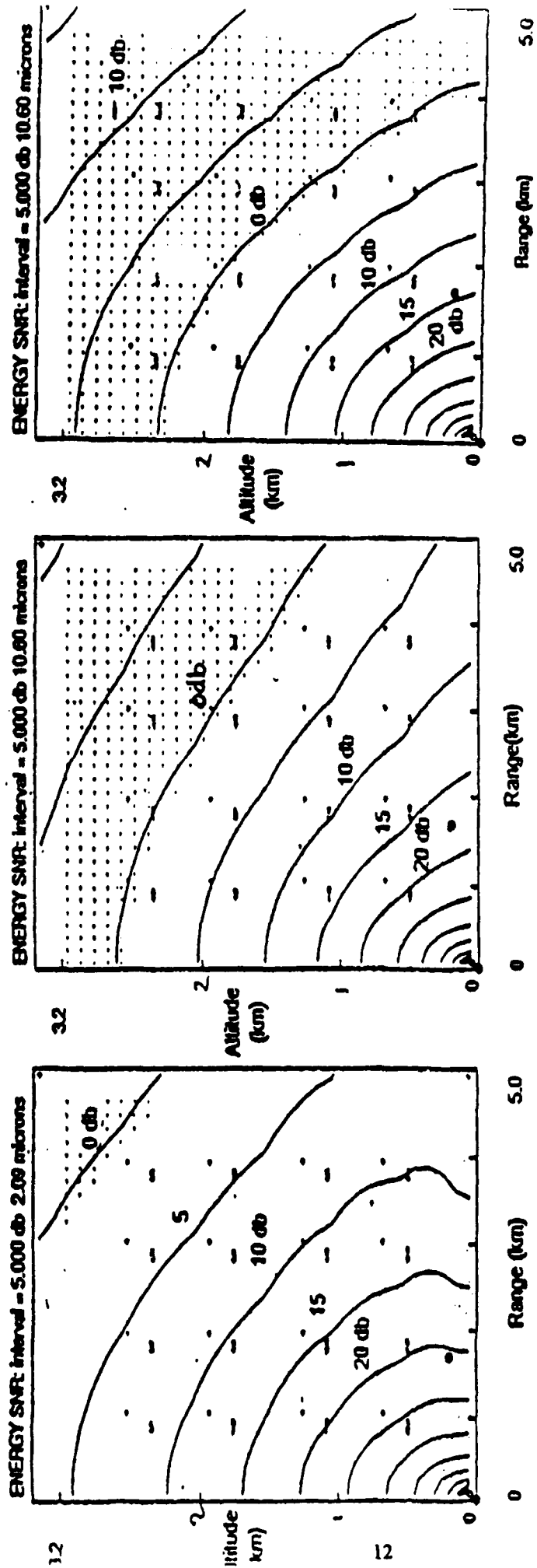
Figure 1.5 Expected SNR levels for a candidate measurement. (Mean power 2 watts, 320 pulses/second, 0.1 meter aperture, clear midlatitude atmosphere, light turbulence. (a) 2.09 microns summer, (b) 10.6 microns winter, (c) 10.6 microns summer. Range and altitude in kilometers. 5 db contour interval.

40 x 40 x 40 mesh with an average of 50 meter resolution. The pulse energy is 6.7 millijoules and is 50 meters long.

1.5 PRELIMINARY VELOCITY MEASUREMENTS AND PROCESSING

It would be highly desirable to demonstrate the velocity retrieval process using existent lidar equipment. The simulations shown in Figures 1.2 to 1.3 indicate that a reasonable reconstruction of the vector wind field might be achievable with as few as 6 scan planes. This would correspond to a 36 prf, 0.25 watt system.

Horizontal scan plane

Vertical scan plane
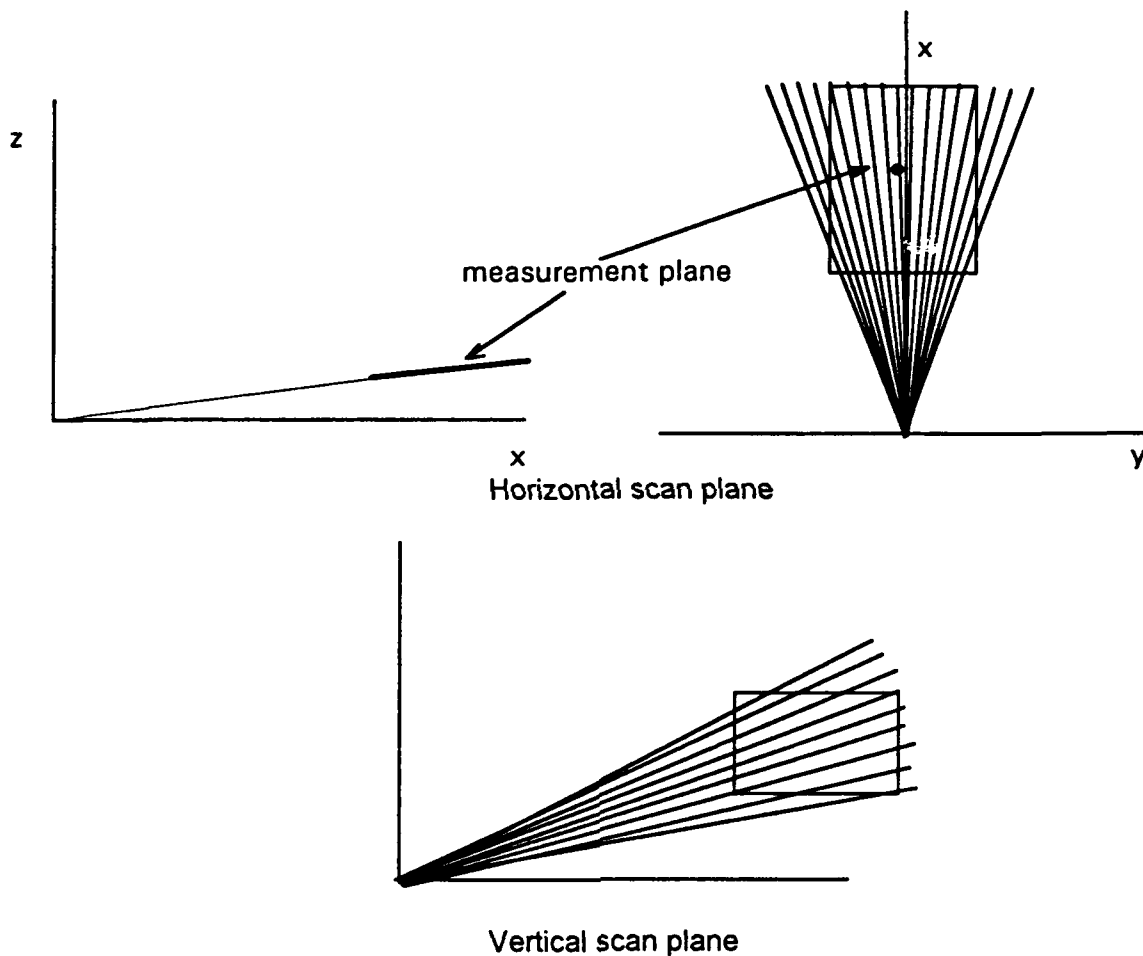
Figure 1.6. Single plane measurement geometries

A scanning lidar with even this capability is not presently available although adequate systems are currently under development. However, two lidars of lower prf are available and have been used to collect data that can be used to demonstrate the data quality and some of the proposed processing concepts.

Two sets of data have been collected. These are described in some depth in Section 4 and are summarized here.

The first data set was collected using a flash lamp pumped 2 micron laser operating at 5 Hz prf. In these data a single, almost horizontal plane was scanned azimuthally over about 90 degrees and the data processed to show the Doppler signature vs range at one azimuth as well as the radial velocity vs range and azimuth. A second data set was collected using a flash lamp pumped 1 micron laser operating at 10 Hz. This latter data, taken at a different location, scanned a sector of a vertical plane in a nodding type of scan. (These pulsed solid-state coherent lidar systems were developed on U.S. Air Force contracts. The technical contract monitor for these systems is Richard D. Richmond, Wright Laboratories in Dayton, Ohio.)

Figures 1.7a and 1.7b show two examples of wind velocity measurements made with the 2 micron system. Figure 1.7a is a plot of the signal frequency content (spectrum) versus range along a single line of sight. The lidar was pointed slightly above horizontal (+3° elevation angle) toward a distant hillside. A Fast Fourier Transform (FFT) is used to construct a frequency spectrum in each of 64 96 meter range gates. The red regions indicate the location in frequency and range of the energetic portions of the signal returns. The blue regions indicate the absence of signal and are due to the local oscillator shot noise floor. The total dynamic range (blue to red) is 60 db. At a range near 5 km, an extremely strong return centered about 0 MHz indicates the distant hillside. A majority of the aerosol returns are centered near -6 MHz and indicate a radial wind velocity of +6 m/sec (positive velocity away from the lidar). Note the interesting velocity structure within the first 2.5 km, especially the 5 MHz (5 m/sec) shear from 1.4 km to 1.9 km.

In Figure 1.7b, the first Doppler spectral moment (velocity) is plotted versus range in a rectangular, side-looking PPI display. For this plot, the lidar scanned through 90° in azimuth with the elevation angle held constant at +3° (this data was collected on a different day from that in Figure 1.5). The color lookup table at the bottom of the screen extends from -8 m/sec (blue) to +8 m/sec (red). (Positive velocities are defined as those away from the lidar). Over the 90° azimuth scan, the radial wind velocity shifts from values near +3 m/sec to values near -7 m/sec. From an azimuth angle of 90° to an azimuth angle of 135°, interesting small-scale (1 to 2 m/sec over ranges of 200 to 400 m) wind eddies are clearly present.

Figure 1.9 shows the second set of data which was taken with the one micron system set to scan a sector in a vertical plane. This system operates at a higher prf (10 Hz) with 80 millijoule pulse energy and used a 0.2 microsecond pulse. This system is beginning to approach the 36 Hz system requirement quoted above. In Figure 1.9 the data have been processed to show both Doppler mean velocity and backscatter intensity vs range for successive pulses as the scan executed a nodding pattern in the vertical direction The mean velocity was calculated using a pulse pair algorithm and each point represents the average of about 10 pulses. The scan cycle is clearly evident in both the intensity and the velocity data. (The strong stationary feature located at about 1 km range is an artifact echo which resulted from a system fault at the time of the data collection).

These data were taken during an experiment to measure aircraft wake velocities. Figure 1.10 shows a contour plot of the line of sight velocity seen in the vertical plane with this system (a different data set than that in Figure 1.9). The quantity shown is the

Figure 1.7a Local Fourier transform vs range at 2 microns

Figure 1.7b Doppler first moment vs range and azimuth at 2 microns

velocity - PP
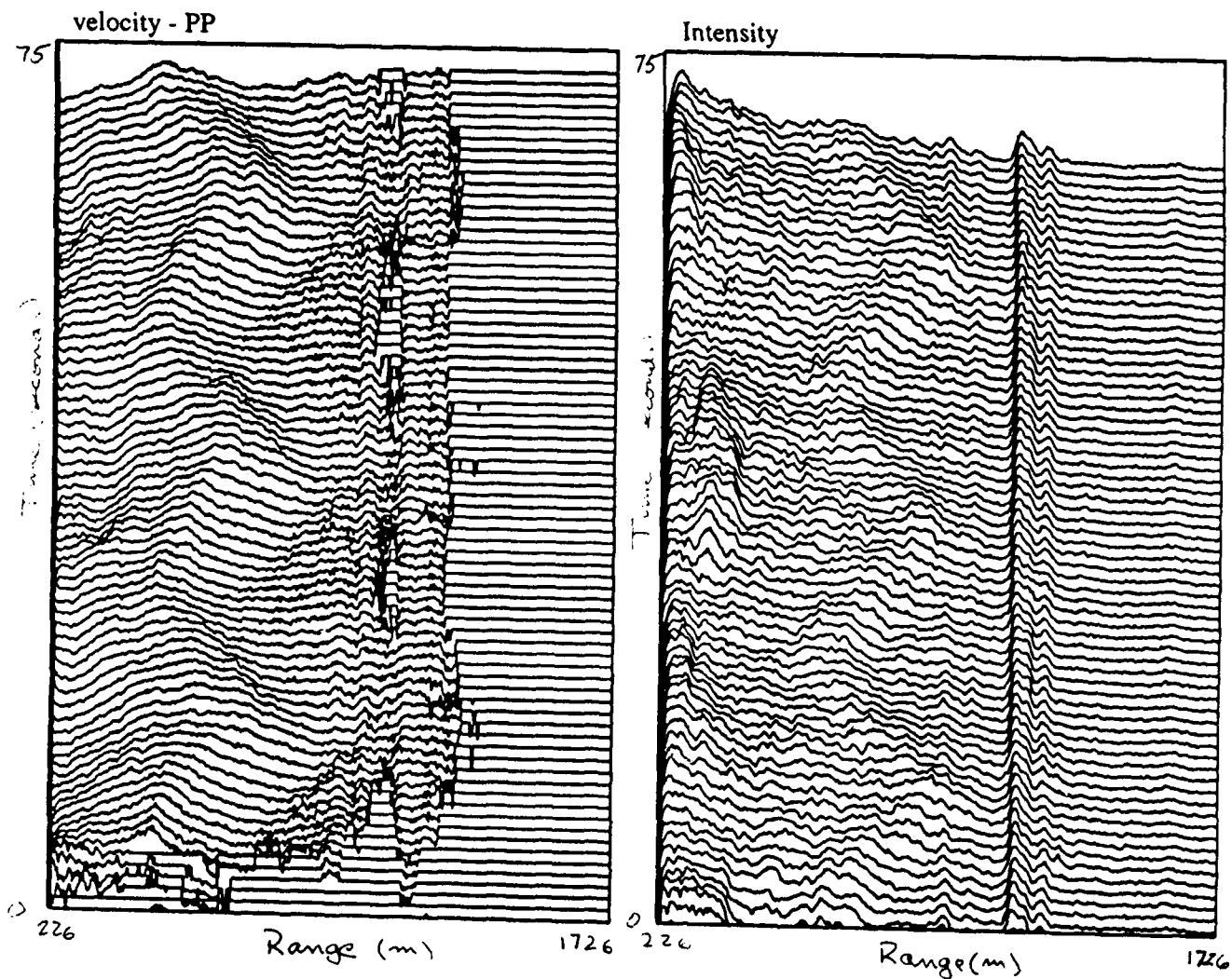
Intensity

Figure 1.9 Pulse - pair estimates of velocity and backscattered intensity vs
range at 1 micron. Every tenth pulse is shown as the elevation angle of
the look direction is scanned through a 9 degree sector between 18 and
27 degrees. The pulse covariance is averaged over 10 successive
pulses (1 second at the 10 Hz prf) before application of the pulse pair
alogorithm. The range extent shown is approximately 1.5 km. The zigzag
pattern is due to the oscillating scan (20 second period-linear profile) as
the line of sight sweeps through the vertically sheared atmosphere. The
strong feature near 1 km is an artifact.

17

B707
Mean Elevation Angle 24°

Contours: Max 0 m/sec
Min −5 m/sec
Delta 0.25 m/sec

LOS RANGE (km)

TRANSVERSE RANGE (km)

Fig. 1.10

18
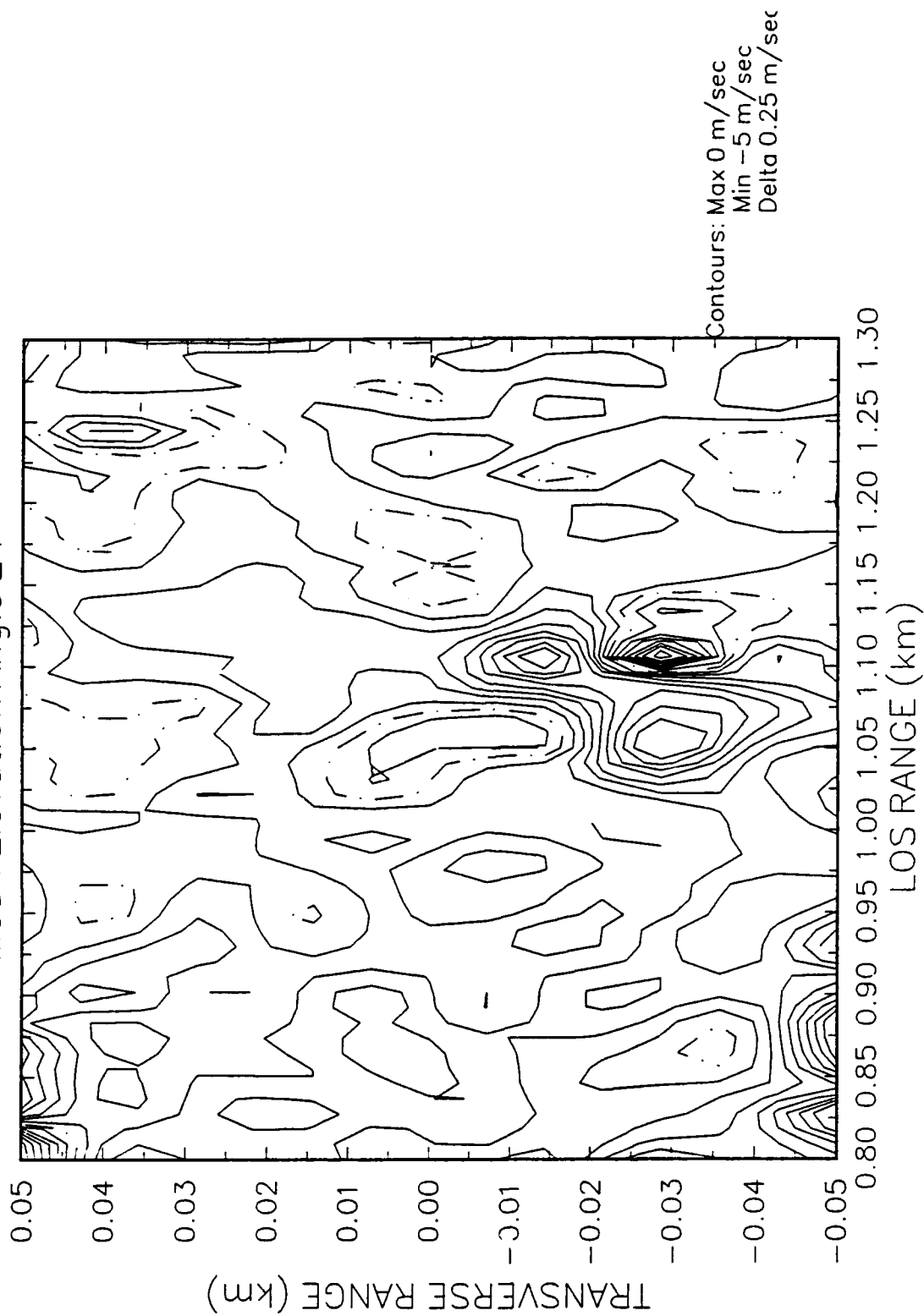
first moment of the Doppler spectrum in successive 30 meter range gates and is plotted as a function of range and crossrange in the measurement plane. The strong feature evident in the lower right of the plot is the vortex wake of a Boeing 707 aircraft which passed through the scan plane a few seconds earlier. It is evident from this figure that velocity structures having scales as small as 25 meters can be resolved with this one micron system.

The preliminary measurements described above demonstrate that both the two micron and the one micron system have the basic capability to acquire velocity data with the characteristics needed for the boundary layer analysis. The principal additional need for a full PBL analysis is to achieve pulse repetition rates up to several hundred Hz. Diode pumped laser systems are currently being developed at CTI that have this latter capability.

System Performance and SNR Model Validation

The accuracy with which the wind velocities can be inferred from lidar measurements depends primarily on two quantities: the system SNR and the Doppler spectrum width. Both of these quantities depend on the atmospheric scattering and propagation properties as well as on the lidar system parameters. CTI maintains an extensive set of simulation and prediction codes for predicting the performance of coherent lidar systems operating against atmospheric targets. The utility of these models relies heavily on how well atmospheric parameters are known both horizontally and vertically. The atmospheric parameters of interest are the volume backscatter coefficient, the atmospheric extinction coefficient, and the refractive turbulence structure coefficient.

Table 1 shows an example of a comparison of measured values of SNR with those predicted by the model. The 2.09 mm, 21 mJ, 5 Hz, 10 cm aperture (8 cm e^{-2} intensity diameter) system was employed for these measurements during a recent Wright Laboratory-sponsored program. The skies were overcast during the measurements, so that refractive turbulence effects should be small (although no direct, quantitative measurement of refractive turbulence was made). For comparison purposes, model predictions for the standard refractive turbulence structure coefficient model (Hufnagel) are given in addition to this same model reduced by a factor of 0.01. As expected, the latter, 'weak' turbulence model predictions better match the measured values. The agreement is quite good for all elevation angles and all ranges.

1.6 DEVELOPMENT PLANS

The demonstration measurements acquired during this study together with the predictions of performance and the development of the vector wind and water vapor correlation processing indicate that three dimensional profiling of the vector wind and water vapor concentration from a single lidar station of the time dependent planetary boundary layer at resolutions of 25 to 50 meters should be possible. Two new processing concepts have been proposed for this analysis and these will need to be evaluated. A program to develop such a boundary layer probe is outlined in the last

Table 1
SNR MODEL VALIDATION — PRELIMINARY
OVERCAST SKIES

ELEVATION ANGLE	RANGE (km)	PRED. SNR_N (dB) Standard C_n^2	PRED. SNR_N (dB) 0.01*(Stand. C_n^2)	MEAS. SNR_N (dB)
0°	1	21.0	27.5	25.1
	2	12.7	25.2	21.5
	4	3.6	20.2	17.1
	6	-2.0	16.0	14.7
	8	-6.2	12.6	12.2
2°	1	25.1	27.4	28.1
	2	19.6	25.0	23.2
	4	11.9	20.1	17.5
	6	6.4	15.9	15.7
	8	1.9	12.3	13.8
5°	1	25.8	27.0	27.2
	2	21.0	24.4	23.6
	4	12.7	18.8	19.3
	6	6.3	14.0	14.3
	8	1.1	9.9	10.5
10°	1	25.7	26.4	27.9
	2	20.8	23.2	25.4
	4	11.5	16.8	11.9
	6	4.1	11.2	11.0
	8	-1.8	6.5	10.7
20°	1	24.8	25.3	28.7
	2	19.2	21.2	13.9
	4	8.3	13.2	11.4
90°	2	12.7	14.4	14.7

λ = 2.09 μm; D = 8 cm (e^{-2} intensity diameter); E_T = 21 mJ; τ = 220 ns; η = 0.1
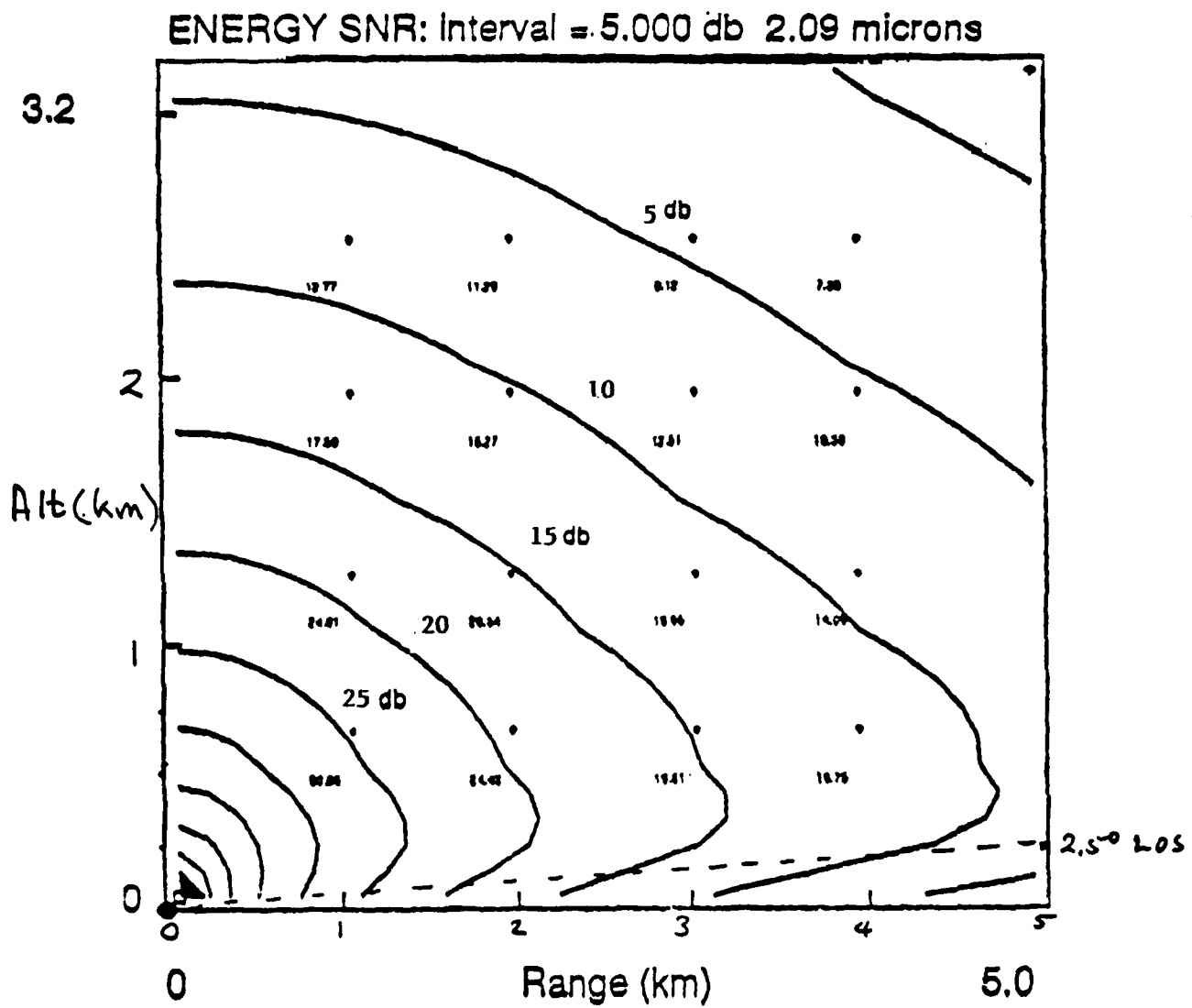
Figure 1.8. Expected Signal to Noise for a 7 millijoule, 0.3 microsecond pulse at 2.09 microns. Midlatitude winter atmosphere, light turbulence, 0.1 meter aperture

section of the report. The program requires the construction or acquisition of a 1 or 2 watt mean power, pulsed diode pumped laser that can operate at several hundred Hz. The expected SNR for a candidate boundary layer measuring system (approximately 7 millijoules at 2.1 microns with a 0.3 microsecond pulse and a 0.1 meter aperture) is shown in Figure 1.8 as a function of range and altitude(midlatitude winter clear atmosphere, light turbulence). SNR values exceed 10 db to ranges of 4 km and altitudes exceeding 1 km and provide an accurate velocity measurement capability in this region.

2.0 MEASUREMENT CONCEPTS

2.1 OBJECTIVES

The objective of the study has been to evaluate the capability for a scanning coherent pulsed laser to acquire high resolution mapping of the three dimensional structure of wind velocity and water vapor in the turbulent planetary boundary layer. This information is needed to obtain a better understanding and modeling of the turbulent transport mechanisms within the boundary layer to support the development and improvement of subgrid models for the transport that can be used in large scale eddy simulations of the turbulent motion.

2.1.1 MEASUREMENT CONCEPTS

A coherent lidar senses the component of the motion of the atmosphere parallel to its instantaneous look direction. To infer vector winds it is necessary either to have multiple looks at each point in space from different directions. or to invoke prior knowledge that the atmospheric motion is sufficiently constrained by the requirements of mass, momentum and energy conservation that the full vector field can be determined from measurements of a single component. We assume that a 3D volume of atmosphere is scanned from a ground station or an aircraft. To determine the vector wind at each point in space without making any assumptions about the atmosphere, three separated lidars would be needed to deduce the 3D wind vector at each observation point. It is the conclusion of the present study that winds in the actual atmosphere are sufficiently constrained by the rules of fluid mechanics that the same capability can be achieved under most circumstances with a single lidar which senses only the instantaneous component of velocity parallel to the line of sight. By making such measurements quasi continuously in time over a 3D volume of space and by making use of known or assumed constraints on the motion, the vector information can be retrieved.

This basic approach has been well developed in radar meteorology where data acquired with two separated radars, viewing a common storm volume is combined with the constraint of fluid continuity to yield the 3D distribution of wind vectors throughout

the storm environment[1] Similar applications of momentum constraints have been applied to radar interrogation of storm clouds from fast moving aircraft(3,4). Based on the results of the present study, we feel that extensions of these techniques are appropriate for lidar observations of the planetary boundary layer. In particular we feel that 3 dimensional scanning measurements made from a single platfrom, either ground or airborne, can be processed to yield a 3 dimensional description of the wind vector field in the turbulent boundary layer. The ability to do this relies on having three elements in the processing: 1) an accurate model of the measurement process (i.e., how the speckled Doppler data is related to the scattering and motion of the aerosol scatterers in the focal volume), 2) a realistic mathematical description of the three dimensional fluid dynamics of the hydrodynamic constraint, and 3) a well founded algorithm for merging these models with the data.

In this report we will outline the proposed measurement and processing concepts and provide estimates and simulations of expected performance for candidate measuring geometries.

The correlation of the vector wind field with the distribution of passive constituents, particularly water vapor, is key to the understanding of energy transport in the convectively turbulent boundary layer. DIAL (DIfferential Absorption Lidar) is a technique which senses spectral differences due to water vapor absorption in displays of backscattered lidar energy. In principle data from a scanning DIAL system can be processed to yield a description of the 3D spatial structure of the water vapor mixing ratio at the same scales as the wind field measurements. However, DIAL as it is normally implemented, is very insensitive to structure scales that are much less the overall scale of the absorbing path. Thus it is most useful for describing the large scale distributions of the absorbing species. In this study we have developed a modified DIAL concept which relies on correlations of the water vapor fluctuations with fluctuations in the density of natural aerosols over a range of spatial scales. By using DIAL to sense the correlation between aerosol and water vapor fluctuations at large scales plus direct measurements of aerosol fluctuations at the smaller turbulent scales, the water vapor fluctuations at both large and small scales can be estimated. When combined with simultaneous, colocated velocity measurements, the turbulent fluxes of moisture and latent heat can be evaluated.

In this report we will identify a suitable measurement and processing system for measuring the combined water vapor - velocity field and outline a candidate measurement program to confirm the concepts.

2.1.2 MEASUREMENT OF VECTOR WINDS

We consider two basically different measurement concepts: one from an aircraft that flies over or under the region to be surveyed, and the other a ground installation that views the atmosphere above and around the lidar installation. To deduce a three component wind vector at each point in space from measurements of one component, at least two additional conditions must be imposed. In the present analysis these will be the requirements of continuity and of momentum conservation.

Mass conservation requires that the deduced velocity vector field be divergence free, i.e., that the equation of continuity is satisfied:

$$\frac{\partial u}{\partial x} + \frac{\partial v}{\partial y} + \frac{\partial w}{\partial z} = 0 \qquad (1)$$

where u,v,w are the three velocity components corresponding to the directions x,y,z (we use the convention that z and w are in the vertical direction). Measurements of two components of velocity over the entire 3D space plus this equation allow the full reconstruction of the vector field.

This method has been used with great success in radar measurements of storm structure (Dual Doppler method). Here measurements of the line of sight velocity of a storm region are made simultaneously from two different ground stations. When combined with Eq. (1) together with the boundary condition that the vertical velocity vanish at the ground surface, the 3D distribution of vector winds can be reconstructed.

An example of such a 3D vector wind retrieval is shown in Figure 2.1. Since the radars view the atmosphere continuously, a 3D motion picture of the vector wind field can be constructed by this method. This technique has been very useful in eliciting understanding of the detailed dynamics of severe storms and their generation of low altitude wind shear. In principle the same procedure can be applied to lidar using two spatially separate systems that conduct a coordinated scan of a common atmospheric volume.

The Dual doppler method requires two separate ground stations. An approximation to such a multi view system with a single radar or lidar can be accomplished on board a fast moving aircraft. This technique has been proposed and implemented by a number of experimenters for radar observation of local storms from aircraft.

In this flyby mode the aircraft scans the 3D field above or below (or around) the aircraft as it flies past the atmospheric volume to be scanned. As long as the aircraft speed is much greater than the atmospheric motions being observed, the atmosphere can be assumed frozen in its motion for the period required for the aircraft viewing aspect to change substantially. Roughly speaking, the aircraft speed should be many times larger than the product of the rms atmospheric velocity fluctuations and the ratio of the overall dimension of the absorbing region to the spatial scale of the fluctuations of interest:

$$V >> (R/l)v \qquad (2)$$

Vertical and Horizontal Winds, 1411 CST   Reflectivity, 1411 CST
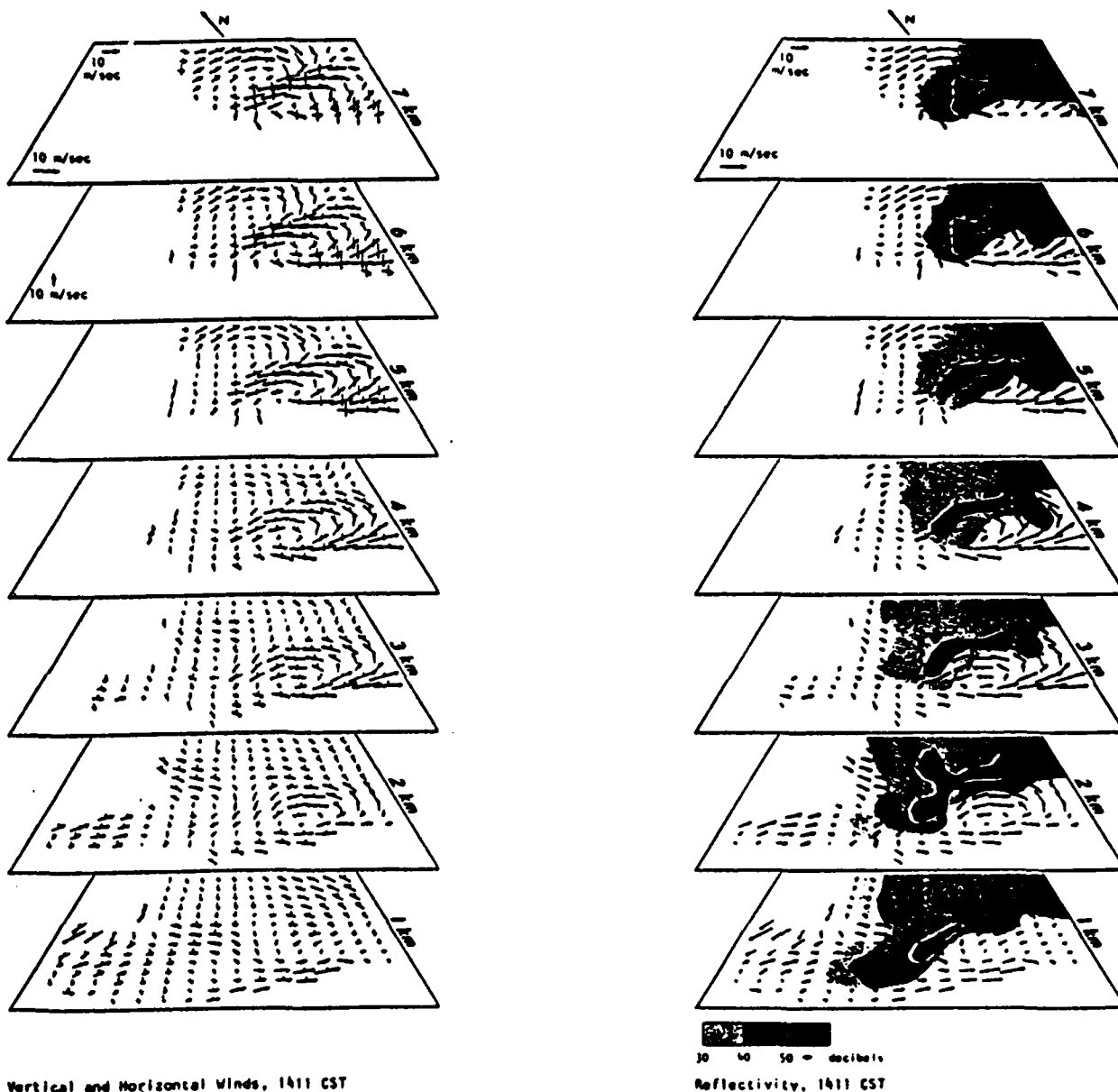
The latest instrument in severe thunderstorm research is dual Doppler radar. Data from two Doppler radar sets aimed at a single thunderstorm can be used to reconstruct the three-dimensional flow patterns as shown for a storm that occurred in Oklahoma on June 8, 1974. These data revealed the development of a double vortex inside a supercell thunderstorm as a tornado extended to the ground. The radar reflectivity patterns at 2 km show the hook echo in relationship to the rotation of the mesocyclonic vortex that contributes to its shape (from J. R. Eagleman and W. C. Lin, "Severe Thunderstorm Internal Structure from Dual Doppler Radar." *J. Appl. Meteorology.* October 1977)

Figure 2.1 Dual Doppler Radar Reconstruction

Here we take the range R as a measure of the outer scale of the viewed region and l and v to be the fluctuation scale and velocity respectively. This condition states that, in order to freeze the motion, the rotation rate of the viewing line of sight (V/R) must greatly exceed the physical rotation rate of typical fluid elements at the measurement scale (v/l). For V=150 m/s and v=5 m/sec, this requirement will not be met for fluctuation scales much smaller than a third of the range. Thus application of this method must be viewed with caution for following intensely turbulent features and may in fact not be very reliable for most turbulent structures. It is most appropriate for diagnosing very weak turbulence structures (<1 m/s fluctuations) or for eliciting the large scale motions of storm regions.

From a single ground station the same 'frozen' structure approach can be applied if it is assumed that the atmosphere drifts past the observing station without sensible change in its small scale structure. Here the mean drift velocity replaces the aircraft velocity in Eq. (1). The region of applicabilty of this method is very limited for a ground station unless it is known a priori that small scale, long-lived advecting patterns are present.

A better approach to the interpretation of data from both a single ground station or from an aircraft platform can be achieved if a more physical account of the advection process is used. Here, instead of invoking a 'frozen' turbulence assumption, a requirement that the observations be consistent with conservation of momentum is to be imposed. This constraint can be imposed by demanding that, in addition to satisfying the continuity equation, the inferred velocity field also satisfy momentum conservation equations. In the limit of rapid but steady advection of a slowly changing atmosphere this constraint reduces to the frozen advection assumption. However, since it is applicable to the atmosphere as observed from platforms moving at any speed, including zero, it has a much greater range of applicability. This approach has been used in this study. The mathematics of its invocation are discussed in detail in Section 3.1.

2.1.3 MEASUREMENT OF WATER VAPOR USING DIAL

Transport of water vapor in the atmosphere is a vital component of the atmospheric dynamics. Latent heat release or extraction as water condenses or evaporates is an important and often dominating source of temperature change and the buoyant forces that drive the convective motions in unstable boundary layers. The upward transport of energy is determined by correlations between water vapor fluctuations and fluctuations in the vertical velocity. The goal of the present study is to evaluate the potential of using lidar to monitor simultaneously both of these quantities at scales as small as 20 meters.[2] Differential absorption of the lidar energy scattered from natural aerosols (DIAL) is a technique to deduce the presence and spatial distribution of an absorbing species by comparing the amplitude of the backscattered light at two different, but closely spaced, wavelengths where the extinction coefficients differ substantially but for which the scattering coefficients are virtually identical.

---

[2]The estimates presented later in this report indicate that estimation of the velocity with submeter per second precision may limit the spatial resolution to somewhat larger values (25 to 50 meters).

Figure 1.4a shows the absorption coefficient of a midlatitude summer atmosphere at ground level in the neighborhood of 2.01 microns; Figure 1.4b shows the absorption coefficient due just to water vapor alone. With a Tm:YAG laser any wavelength in the spectral region indicated can be selected by electronic tuning. In the DIAL technique using a pulsed laser, two wavelengths are alternately selected at successive pulses or intervals: one in the vicinity of the center of an absorbing line and one immediately adjacent where the absorption coefficient is substantially smaller. To achieve maximum sensitivity, the absorption coefficient should be chosen so that the extinction in the absorbing channel is about a factor 2 or 3 at the center of the region to be diagnosed; i.e., so that the absorption coefficient is comparable to the inverse of the mean range.

As an example, one such line for the Tm:YAG laser is marked in Figure 1.4. The center of the line is located at 2.016974 microns. Since the line half width at half maximum is 2.8 GHz/atm, a separation greater than 3 GHz is suitable for the non-absorbing wavelength. At 2.017713 microns (5.8 GHz separation) there is a minimum in the total absorption equal to about 0.1 per km. At one atmosphere pressure, the absorption coefficent at the line center is about 3.4 per kilometer (midlatitude summer atmosphere). Thus two wavelengths can always be selected in this region that will be optimal (i.e., for which the absorption coefficient of the stronger line is of order 1/range) for a DIAL measurement of water vapor for any nominal range between a few hundred meters to more than 5 km.

Two pulses, closely spaced in time, are to be transmitted, one at each wavelength. In expectation the return signal intensities at the two wavelengths will have the form

$$I_1(x) = I_o(x)\beta(x)\exp(-2\int_0^x k_1(x')dx')$$

$$I_2(x) = I_o(x)\beta(x)\exp(-2\int_0^x k_2(x')dx')$$

(3)

Here $I_o(x)$ contains the geometry factors associated with the illumination and reception and $\beta(x)$ is the local backscatter coefficient (both assumed identical at the two wavelengths). The local absorption coefficient difference (and therefore the local water vapor density or mixing ratio) is evaluated as a function of range (in the absence of noise) by differentiating the logarithm of the ratio of these two signals:

$$\Delta k(x) = k_1(x) - k_2(x) = \frac{1}{2}\frac{d}{dx}\ell n(I_2(x)/I_1(x))$$

(4)

With finite noise a least squares formula should be used:

$$\Delta k(x) = \frac{1}{2}\frac{d}{dx}\ell n(< I_2(x)I_1(x) > / < I_1(x)^2 >) \tag{5}$$

In Eq.(5) the brackets (<>) represent an average over successive samples or neighboring range gates.

The DIAL measurement is limited by the noise in the intensity channel, especially when high spatial resolution is desired. This noise is due to speckle at high SNR and is photon shot noise at low SNR. The expected fractional error (standard deviation) of the measured absorption coefficient is given approximately by (5)

$$\frac{\delta k}{k} = \frac{1}{k\Delta\sqrt{N}}\frac{\sqrt{1+SNR^2}}{SNR} \tag{6}$$

Here Δ is the resolution width and N the number of independent samples contributing to the estimate. At large SNR and for an optimum level of absorption($k\sim1/L$), the rms precision (dk) of the inferred absorption coefficient is given by

$$N = \frac{(L/\Delta)^2}{(\delta k/k)^2} \tag{7}$$

For meteorological estimates a precision of the estimate of the local water vapor content of the order of 10% (standard deviation) or better is probably necessary. Using DIAL, even with optimum choice of absorption coefficient, a very large number (10^4 to 10^5) of independent samples per resolution element will be needed to achieve a useful measurement of water vapor fluctuations at scales less than a tenth of the range. Thus the DIAL technique is best applied to estimating relatively coarse grained averages.

It is very difficult to achieve such high levels of averaging while maintaining high detection efficiency with a heterodyne detection system. Without defocusing each pulse is limited to providing one or at most a few independent samples (depending to the degree velocity spread within the pulse length). In order to achieve such high levels of averaging it is necessary to detect a very large number of incoherent scatterers within each resolution field to reduce the speckle noise. Illumination with spectrally and angularly defocused or broad laser pulses and using direct (non-coherent) detection of the total backscattered energy is required. Even so the averaging requirements can be severe when high spatial resolution is desired (see Section 2.1.4).

In view of the above considerations we have concluded that the DIAL technique *as conventionally implemented* does *not* provide a useful method with a coherent lidar using heterodyne detection for measuring spatial distributions of water vapor fluctuations at small turbulence scales. DIAL is most appropriate to the sensing of moderate to large scale features (>10% of the overall dimension).

Alternative strategies include direct detection of the backscattered energy from non coherently illuminated scatterers in each resolution volume or correlation of the water vapor fluctuations with the more readily detected aerosol fluctuations. These will be discussed next.

2.1.4 MEASUREMENT PRECISIONS : Aerosol scattering intensity and DIAL

It is informative to examine how the energy and prf requirements for a DIAL measurement of the density distribution of an absorbing species and direct measurements of the local backscattering coefficient depend on the spatial resolution of the measurement.

We assume that a 3D volume of dimension L is to be scanned in a specified time T with a 3D resolution Δ. Two sources of noise contribute: speckle and photon shot noise.

Photon Shot Noise Only

The total number of photons that must be incident on the interrogated volume during the dwell time to achieve the desired rms detection precision ε of the scattering coefficient β_{sc} is proportional to

$$N_{scatt} = G \frac{1}{\varepsilon^2} \frac{1}{\beta_{sc}\Delta} \left[\frac{L}{\Delta} \right]^2 \qquad (8)$$

where G is a factor determined by the collection geometry.

In a ideal DIAL measurment we would choose the absorption coefficient to be approximately equal to 1/L. For this choice the number of photons that need to be incident to achieve the same precision in the measurement of absorption coefficient is equal to

$$N_{abs} = G \frac{1}{\varepsilon^2} \frac{1}{\beta_{sc}\Delta} \left[\frac{L}{\Delta} \right]^4 \qquad (9)$$

i.e. a factor of $(L/\Delta)^2$ larger. This additional factor in DIAL results from the fact that the DIAL measurement must difference adjacent range cells to get the absorption signature whereas the backscatter is a direct measurement. Thus when photon noise dominates it is much easiest to measure the mean scattering coefficient than it is to measure the absorption coefficient. When speckle dominates, this proportionality and these formulae still hold as long as N is interpreted as being the number of independent samples acquired, not the number of photons incident.

Because of the very strong dependence of required power and number of independent samples on spatial resolution for the DIAL measurement ($N \approx 1/\Delta^5$) we can expect

that DIAL measurements will be restricted to relatively coarsed grained averages in space.

2.1.5 DIRECT DETECTION DIAL

Direct (incoherent) detection lidar systems detect the backscattered electric field intensity and do not retain phase information. Because they are intensity-only detection systems, wavefront distortions due to atmospheric refractive turbulence only negligibly reduce system SNR. Consequently, these systems are able to employ significantly larger apertures (50 cm and more) without turbulence-induced coherence loss effects. Furthermore, by using a transmit aperture that is much smaller than the receiver aperture, direct detection systems are able to reduce and effectively eliminate laser speckle effects. The transverse size of laser speckle lobes at the lidar is approximately equal to the transmit aperture size. The larger receiver aperture collects backscattered radiation from several speckle lobes simultaneously and thereby 'aperture averages' out the speckle-induced intensity fluctuations. The number of speckle lobes that can be averaged with direct detection lidar systems, or the degree M of aperture averaging available, is proportional to the ratio of the receiver aperture area to the transmit aperture area. For example, a 3 cm transmit aperture with a 48 cm receiver aperture achieves M ~ 256. To achieve this same sort of speckle reduction, a heterodyne detection system would need to average 256 pulses or equivalently, employ a 256 element detector array.

Water vapor measurements with direct detection DIAL has been performed most notably at ruby (694 nm), CO_2 (10 μm), and Alexandrite (725-730 nm) laser wavelengths. One of the primary difficulties with these all of these systems is that they cannot be made sufficiently compact while at the same time providing accurate, high spatial and range resolution, water vapor measurements over sufficiently large areas.

2.1.6 CORRELATION DIAL

An alternate strategy for estimating the water vapor fluctuations utilizes the expected space time correlation that should exist in a turbulent flow between all passively advected constituents, in particular water vapor and ambient aerosols. In this technique DIAL measurements at large scales are used to interpret aerosol density measurements at small scales in terms of estimates of water vapor fluctuations.

The basic assumption is that all passive constituents that are advected in the turbulent atmosphere by the same flow mechanics will have a similar and coherent distribution of fluctuations over a range of scales. This requirement probably limits the applicability of the method to clear or hazy atmospheres that are free from clouds or fog. Evaporation and condensation of water droplets near or in clouds may degrade the correlation between the net backscattering coefficient and the water vapor absorptivity.

Given that the uniform passive advection assumption is valid, a transfer function between water vapor fluctuations and aerosol density fluctuations can be established at large scales where fluctuations of both constituents can be measured with reasonable accuracy. As was shown in Section 2.1.4 the fluctuations of the scattering intensity of the aerosols are much more readily measured at small scales with lidar than are the absorption fluctuations. By assuming that the transfer function between these two quantities is independent of scale, the small scale water vapor structure can be deduced from measurements of the aerosol structure by multiplying by the transfer function derived from measurements at large scale.

For a coherent lidar, the measurements of fluctuations of aerosol density at high SNR obey Rayleigh statistics due to speckle. For a quiescent atmosphere, the correlation length(δs) is the pulse or resolution length(Δ). For a turbulent atmosphere the correlation length may be smaller and is determined by the velocity spread within the pulse length.

The expected fractional standard deviation of the local scattering coefficient varies as

$$\frac{\delta \beta}{\beta} = \sqrt{\frac{\delta s}{\Delta}} \frac{1}{\sqrt{N}} \frac{\sqrt{1+SNR^2}}{SNR} \tag{10}$$

The number of samples required to achieve a given precision in the estimate of the scattering coefficient (and therefore of the water vapor density) is given by

$$N = \frac{(\delta s / \Delta)}{(\delta \beta / \beta)^2} \tag{11}$$

Since $\delta s < \Delta$ in general, the number of samples required by this method will be much less than that for direct DIAL (by the factor $(L / \delta s)^2$). This should allow estimation of water vapor fluctuations down to scales limited only by a requirement to achieve an adequate single range gate SNR.

2.2 APPROACH

The proposed approach for measuring water vapor fluctuations simultaneously with wind vector fluctuations may be summarized as follows.

- Radial winds and backscattering coefficients are measured over a 3D volume as a function of time using a single scanning coherent lidar.

- Constraints of continuity and momentum conservation are used to infer the distribution of the vector wind over this volume.

- Using one of several spatial horizontally averaging schemes, mean water vapor and backscattering coefficients are measured and correlated to yield three vertical profiles:a height dependent transfer function, the horizontally averaged mean water vapor mixing ratio, and the horizontally averaged mean backscattering coefficient. These measurements are to be carried out before, during, and/or after the wind vector measurements.

- The water vapor - aerosol transfer function is used to convert the scattering coefficient measurements at small spatial scales to a 3D distribution of water vapor concentration.

3.0 PERFORMANCE MODELING

3.1 SIGNAL PROCESSING AND VECTOR WIND RETRIEVAL

3.1.1 KALMAN FILTER RETRIEVAL PROCESSING THEORY

A full 3D approximation of the Kalman filter wind field retrieval analysis has been formulated analytically(see Appendix). In the following section 3.1.2 we summarize the mathematical formalism for retrieval of vector winds for single station Doppler measurements of the line of sight velocity.

3.1.2 VECTOR WINDS FROM DOPPLER DATA

Two formulations have been analysed: an Eulerian form in which velocity and vorticity are evaluated and tracked on a fixed, prespecified grid, and a Lagrangian form in which a cloud of discrete vortex elements or threads are followed. Flow charts of these procedures are shown in Figures 3.1 and 3.2. The specific analysis for incorporating the lidar observations into the fluid dynamic equations describing the momentum and mass conservation equations of the atmospheric boundary layer follows previous concepts but is fundamentally a new formulation.

The formulation for the Lagrangian mode, whose basic equations are described in this section, has a very convenient structure. It allows a physical interpretation of the data assimilation process in terms of a pseudo scalar potential field that is generated by difference between current measurements and predictions of those measurements based on the currently estimated vorticity state. This pseudo field creates an additional velocity field that causes the vorticity state to adapt to the measurements at the same time that it executes the normal hydrodynamics.

Estimates of the computational requirements for 2D and 3D implementations have been made and are described in Figure 3.1.3. The algorithm is relatively efficient and computational loads relatively modest for restricted grid dimensions.

The computation using the Lagrangian mode has been implemented in a 2D numerical simulation. The basic equations (in 3D form) used are summarized in this section.

The computation tracks the trajectories of a cloud of discrete vortex elements in a three dimensional space. The position, orientation, and strength of each vortex are updated at each time interval. The velocity has two contributions:

$$\frac{d\mathbf{x}}{dt} = \mathbf{u}(\mathbf{x}) + \nabla V(\mathbf{x}, \mathbf{a}) \tag{12}$$

The first (u) is the physical velocity due to all the other vortices and is derived as the curl of a local vector stream function

$$\mathbf{u} = \nabla \times \Psi \tag{13}$$

where the stream function is derived by solving a Poisson equation whose source is the vector vorticity

$$\nabla^2 \Psi = \Omega \tag{14}$$

The vorticity is computed by (vector) summing the strengths of all the vortex elements in a given mesh cell and dividing by the mesh cell volume.

The second velocity term is the gradient of a scalar potential, evaluated at the vortex location which arises from the disparity between the predicted and currently observed data. This scalar potential is the dot product of the vortex strength and an error vector potential function vector:

$$V(\mathbf{x}, \mathbf{a}) = \mathbf{a} \cdot \mathbf{A}_s(\mathbf{x}) \tag{15}$$

The error vector potential $A_S(\mathbf{x})$ is a convolution of the error covariance function $P(\mathbf{x})$ with a pseudo-stream function field Ψ_s which is generated from the measured data:

$$\mathbf{A}_s(\mathbf{x}) = P(\mathbf{x}) * \Psi_s(\mathbf{x}) / R\Delta X\Delta S\Delta t \tag{16}$$

In this equation the asterisk represents a spatial convolution. The error covariance function $P(\mathbf{x})$ arises in the estimation process as an estimate of the uncertainty of the estimated locations of the vortex elements, $\Delta X\Delta t$ and ΔS are volume elements in the state and measurement space respectively, and R is the expected measurement error (variance) of the line-of-sight velocities.

The pseudo-stream function is the solution of a vector Poisson equation for which a pseudo vorticity field Ω_s is the source:

$$\nabla^2 \Psi_s = \Omega_s \tag{17}$$

The pseudo-vorticity itself is calculated from the measured data as the curl of a vector field consisting just of the observed line-of-sight velocities:

$$\Omega_s(\mathbf{x}) = \nabla \times \mathbf{Z}_s(\mathbf{x}) \tag{18}$$

Here the vector field $\mathbf{Z}_S(\mathbf{x})$ is constructed from the lidar measurements of the line-of-sight velocity $\mathbf{Z}_S(\mathbf{x,n})$ as a sum over all lines of sight according to

$$\mathbf{Z}_s(\mathbf{x}) = \sum_n \mathbf{n}\mathbf{Z}_s(\mathbf{x,n}) \tag{19}$$

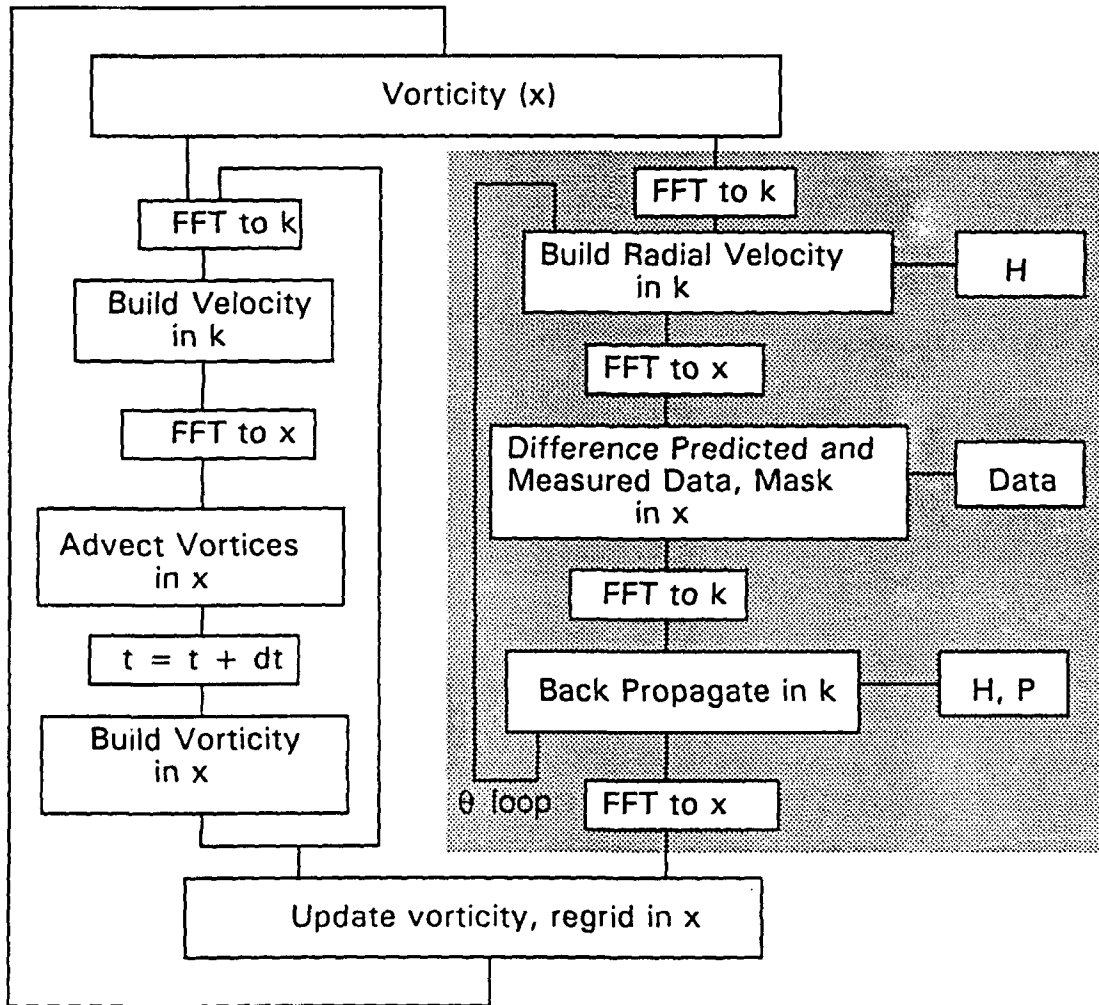where $\mathbf{n}$ is a unit vector in the direction of the given line of sight.
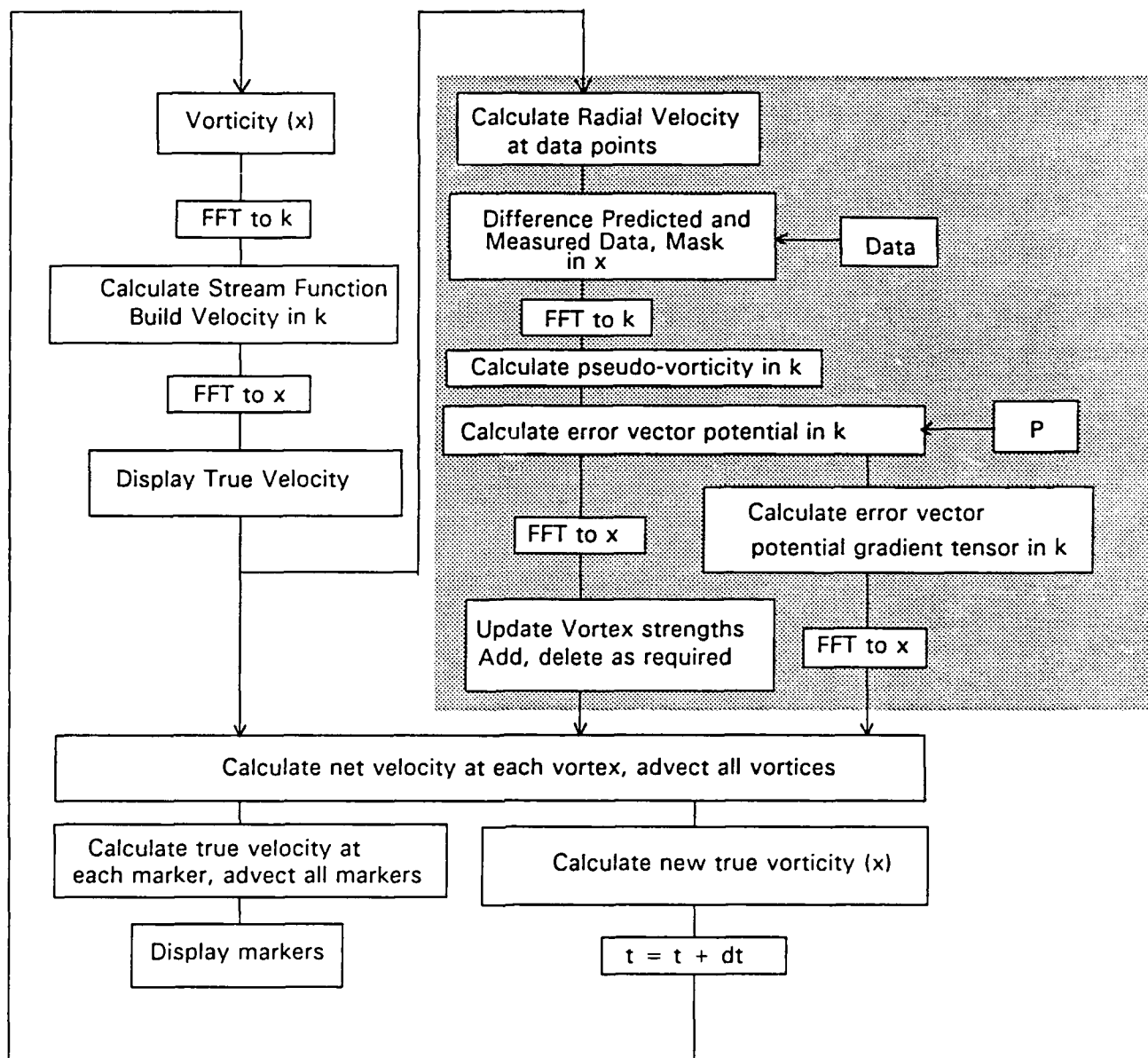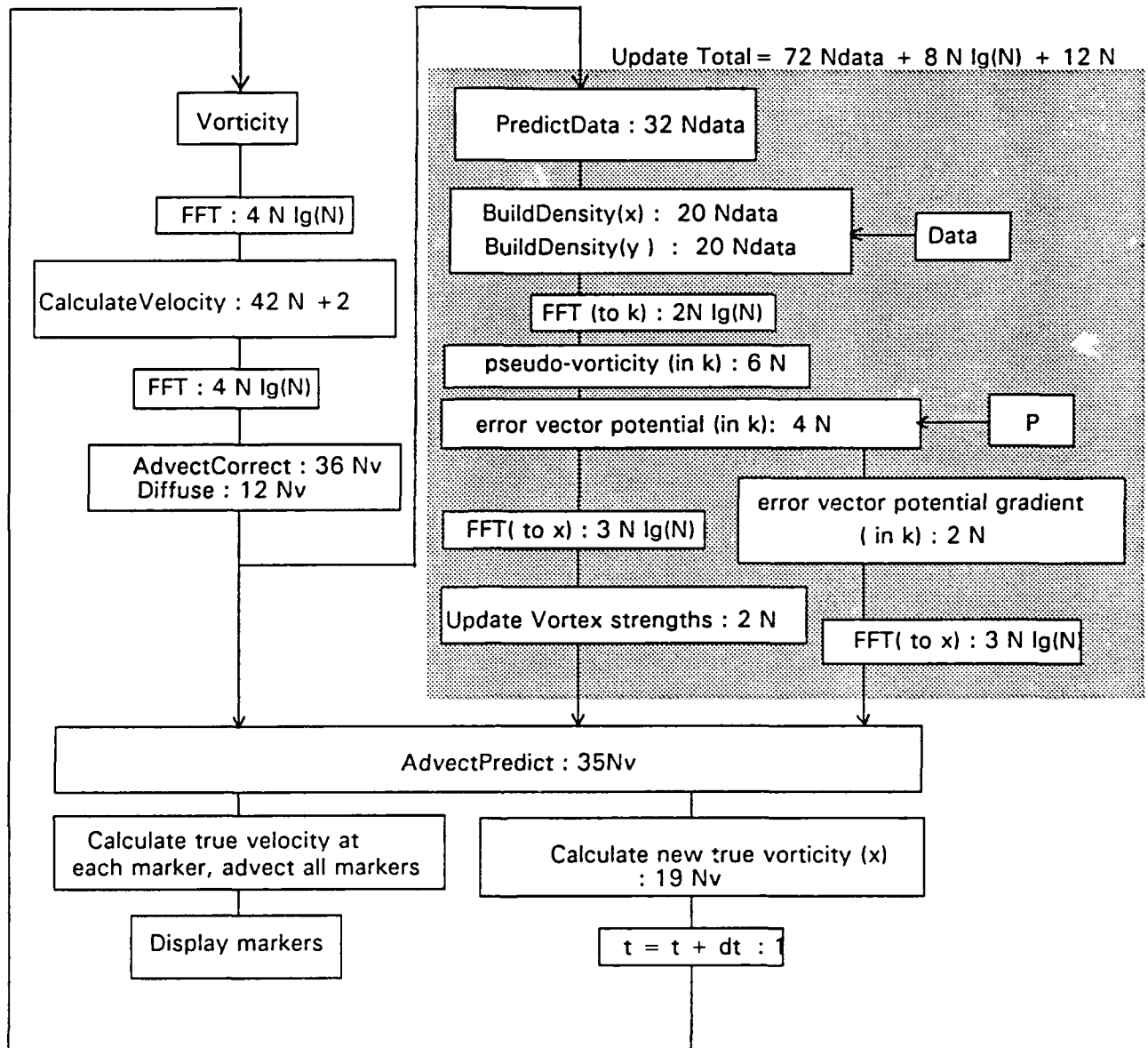

Figure 3.1. Kalman Filter Update Sequence : Eulerian

34

Figure 3.2. Kalman Filter Update Sequence : Lagrangian

Figure 3.3 . Arithmetic operations count for the Lagrangian mode (2D code)

These equations can be used to adapt a preexistent field of vortex elements to a set of measurements while maintaining consistency with the mass and momentum equations of motion of the atmospheric fluid.

In addition to moving the vortex elements to better fit the observations, the Kalman filter can also change their strengths and orientations. The growth rate of the circulation of vortex element **p** is proportional to the negative of the pseudo-stream function

$$\frac{da_p}{dt} = -\frac{\sigma_a^2 \Psi(x_p)}{R \Delta S \Delta t}$$

(20)

where σ_a is the expected rms uncertainty of the estimate of the vortex strength a_p. A detailed derivation of these relationships is provided in the Appendix.

3.2 WIND VELOCITY ESTIMATION: SIMULATIONS AND EXPECTED PERFORMANCE

A previously developed 2D simulation hydro code has been modified to use these Lagrangian mode equations. Here the vorticities and stream functions have only a single component in the direction perpendicular to the simulation plane.

The simulation is used in two steps. First a calculation with no input data is carried out starting from some selected initial vorticity distribution. The radial velocity that would be sensed along selected lines of sight is recorded. This recorded data, modified by the lidar response function and with added noise, is then used as data input for a data assimilation run.

For a demonstration of the process we have constructed the velocity field of a simulated 2D wind gust. Here the initial condition consists of a downward moving parcel of air initially centered at an a altitude of about 700 meters (Figure 1.2). Because of the periodic boundary conditions imposed in the horizontal direction, there are actually a row of wind gusts each separated by the width of the computed field. These gusts impinge on the ground surface at an angle of about 45 degrees and each split into two parts moving in opposite directions. These parcels travel horizontally until they encounter other parcels entering the computational mesh from adjacent periodic image cells. The collision of these parcels then results in an upward travelling jet.

Simulated lidar data is recorded along each of the lidar lines of sight shown in Figures 1.2 and 1.3. The data is derived by convolving the calculated line of sight component of the fluid velocity with the lidar range response function, and adding simulated photon and speckle noise. This data is recorded and is to be input to a second, data assimilation code.

37

Implementation of the Kalman Filter

Computational sequences for Eulerian and Lagrangian modes are outlined in Figures 3.1 and 3.2. In these figures the greyed areas represents the update that results from the incorporation of the measured data, the remainder represents the calculation of the natural inviscid hydrodynamic motion. In both modes the calculation cycle starts with the three dimensional distribution of vector vorticity. At the initial time this distribution can be selected arbitrarily, and is typically set to yield a motionless or uniformly moving atmosphere. This vorticity serves as the source function for a Poisson equation given in Eq. (14). Gradients (the curl) of the stream function solution are evaluated at the location of individual vortex threads to yield the fluid advection velocity. In the absence of measurement input this velocity is used to advect the vortex threads with the local fluid for the given time interval. A revised vorticity distribution is then calculated based on the new vortex positions and the process repeated.

When measurements from the lidar are to be incorporated, the line-of-sight radial velocity is evaluated at each of the range gates using the current velocity field predictions. The difference between these predictions and the measured values are inserted into an x-y grid at the measurement locations and the rest of the grid is set to zero. The Eulerian and the Lagrangian procedures differ primarily in the way these differences are then assimilated.

In the Eulerian calculation mode the 3D data error field is passed through a spatial filter to yield an increment of vorticity at each point in the spatial grid. This vorticity increment field is then added to the current vorticity estimate produced by the most recent hydrodynamic prediction step of the calculation. A new set of discrete vortex elements is then built to represent this updated vorticity field and the process repeated.

In the Lagrangian mode the data errors for different look directions are combined to form a 3D vector error field which consists just of the vector difference between the measured line of sight components of the wind field and their predictions. Only locations and components that actually contribute to the measurements contribute to this vector field; all other velocity values are set equal to zero. The curl of this psuedo-wind field is then used as the source function for a Poisson equation.

The solution of this Poisson equation, after being passed through a second spatial filter, is used for two purposes: First, it serves a source for generating new vorticity. To this point the Lagrangian calculation is, in principle, equivalent to the update process in the Eulerian mode. In the Lagrangian mode, however, the Poisson solution field is also used to create a scalar pseudo-potential whose gradients are added to the physical velocity field and the total used to advect the discrete vortex elements. This allows two methods for the correction: one is the creation of new vorticity, the other is the advection of existent vorticity.

Since the pseudo-potential is equal to the projection of the vortex strength on the vector solution of the Poisson equation, vortex elements having opposite strengths will move in opposite directions in this error correction field. This latter advection allows a preexisting vorticity field to adapt to measurement input without necessarily requiring the creation of new vorticity.

Figure 1.2 shows, as a function of time, the developing inferred vector field produced by the Kalman filter for a wind gust simulation. Figure 1.2a shows the velocity state shortly after initiation of the measurement. In this example the wind field was created by a simple vortex pair representation of a wind gust. Data has been acquired along three lines of sight. In the reconstruction, the inferred atmosphere is assumed to be initially motionless. The Kalman filter then generates and advects vorticity to allow the atmosphere to adapt to the measurements.

The upper panels of each of Figures 1.2a and 1.2b show the inferred wind vectors and the locations of the lines of sight. The six lower panels in each of Figures 1.2a and b show the simulated measured data (solid lines) and the current predictions (dots). Panels containing asterisks are the measured lines of sight. The intermediate panels show true and predicted data along intermediate sight lines. At the time of this first display there are significant differences between the predictions of the radial winds and the measurements along both participating and non-participating lines of sight. The difference between these values drives the adaption process. The adaption that has taken place at this time is due primarily to the imposition of the continuity constraint. With time, both the momentum constraint and the continuity constraint continue to cause the solution field to adapt to the data. Later in time (Figure 1.2b) these differences are reduced to the point that the predictions are effectively identical to the measurements. At this time the modeled atmospheric field is fully consistent with the data as well as with all the hydrodynamic constraints embodied in the fluid equations of motion. At this later time the predicted data field also agrees very well with true radial velocity on the non-participating sight lines indicating an accurate reconstruction of the entire vector field.

Reconstructions of a more complex wind field are shown in Figure 1.3. The true velocity field at time 101 seconds is shown in panel a and reconstructions using 3 and 6 lines of sight in panels b and c. In this case the reconstruction with 3 lines of sight is less satisfactory even though the deduced field at the measurement points is very accurate. With 6 lines of sight the inferred field is well predicted throughout the measurement field.

Examination of these simulations can be used to establish the ability of the retrieval process to reconstruct the wind field solely from radial wind data as the scan strategy is changed. In general the process appears to converge to reasonable approximations of the true flow field if sufficient number of lines of sight are chosen in the vertical plane.

In the Kalman filter analysis as presently implemented, both the constraints of incompressibility and momentum conservation aid the retrieval of the vector wind field from the scalar radial wind measurements. The momentum conservation constraint is basically a method for tracking the advection of persistent patterns of radial velocity. Although not shown in these simulations, detection of patterns of aerosol scattering intensity can also be used to assist the velocity retrieval.

A similar ability to detect and track patterns of absorption of water vapor can be included by incorporating absorption into the measurement model and allowing for passive advection of water vapor in the state description.

Computation Issues

Figure 3.3 shows an approximate count of floating point operations for the Lagrangian mode as implemented in the 2D simulation. One multiply and add is counted as one floating point operation. These numbers were evaluated by counting the operations in the coded 2D calculation used to produce the simulations shown in this report. The count excluded all graphics output as well as any I/O operations. For the sparse lidar sampling selected (6 lines of sight) and the modest number of vortices allowed (on the average a given mesh cell is populated 50% of the time) the computation is dominated by the Fourier transforms required to generate the real and pseudo velocity fields. For this coding somewhat more than 300 operations per spatial mesh point per cycle are required. For the 64x16 mesh, this corresponds to 300,000 operations per cycle expected for the 2D simulation. In 3D the number of operations per mesh point is roughly tripled, since three components of vorticity and streamfunction are required rather than just the one needed in 2D. Thus, for a 64x32x16 mesh, we anticipate a computation load of order 30 million multiply and add operations per cycle. Given that cycle times of one to several seconds are anticipated, the present SkyBolt board used in CTI's signal processor should be (just barely) capable of handling this load in a real time operational mode.

4.0 PRELIMINARY VELOCITY MEASUREMENTS

The 2.1 micron coherent lidar system is currently being integrated into a mobile lidar van (see Section 6.0). Prior to its installation, the system has operated out of a building at CTI's Table Mountain test facilities. The system has a 10 cm aperture and uses a computer-controlled, super-hemispherical scanner to produce Plan Position Indicator (PPI) and Range Height Indicator (RHI) displays. The system transmits 20 mJ/pulse with a pulse repetition frequency (PRF) of 5 Hz and a full width half maximum (FWHM) pulsewidth of roughly 200 nsec (range resolution ~30 meters). The 200 nsec pulsewidth permits the type of high resolution velocity measurements required to understand the dynamics of the turbulent boundary layer.

Signal returns are digitized at a rate of 100 megasamples/sec and processed with CTI's Real Time Lidar Processor (RTLP) and displayed in a variety of formats. Figures 1.7a and 1.7b show two examples of wind velocity measurements made with the system.

Figure 1.7a is a plot of the signal frequency content (spectrum) versus range along a single line of sight. The lidar was pointed slightly above horizontal (+3° elevation angle) and to the north of Table Mountain toward a hillside. In each of 64 equally spaced range gates, a 64 point Fast Fourier Transform (FFT) is computed. The sample spacing is 10 nsec (1.5 m) such that the width of each range gate is 96 m. The FFT amplitudes are color-coded and displayed as a horizontal 'stripe' along the frequency axis in Figure 1.7a. This figure represents one second of data (5 pulses). The range gates (y-axis) cover the line of sight range window from 1 km to 5.54 km. The frequency axis (x-axis) extends from -15 MHz to +15 MHz (or +15 m/sec to -15 m/sec at the 2 micron wavelength). A frequency of 0 MHz corresponds to no Doppler shift and thus implies a zero radial (relative to the lidar) velocity. The color lookup table at the bottom of the screen extends from 10 (blue) to 70 (red) in arbitrary log scale units (a

total range of 60 dB). The red regions indicate the location in frequency and range of the energetic portions of the signal returns. The blue regions indicate the absence of signal and are due to the local oscillator shot noise floor. At a range near 5 km, an extremely strong return centered about 0 MHz is due to the distant hillside. The 0 MHz frequency is expected as the hillside is not moving. Beyond the hillside, no signal radiation is available for detection, and the blue-colored noise floor is all that remains. In front of the hillside, the aerosol returns permit accurate wind velocity estimation. A majority of the aerosol returns are centered near -6 MHz and indicate a radial wind velocity of +6 m/sec (positive velocity away from the lidar). Note the interesting velocity structure within the first 2.5 km, especially the 5 MHz (5 m/sec) shear from 1.4 km to 1.9 km.

In Figure 1.7b, we plot the FFT first moment (velocity) versus range in a rectangular, side-looking PPI display. For this plot, the lidar scanned through 90° in azimuth with the elevation angle held constant at +3°. Please note that this data was collected on a different day from that in Figure 1.7a The y-axis is the azimuth angle and extends from 70° to 160° (90° is due North) and the x-axis is range and extends from 1 km to 5.2 km. Radial velocities are computed from the amplitude thresholded first moment of 64-point FFTs at each of 64 equally-spaced range gates. The FFTs from five adjacent lines of sight are combined to compute each mean velocity output record (five pulse averaging). Each output record is plotted as a horizontal stripe of radial wind velocity versus range. The y-axis location for each horizontal stripe corresponds to the averaged azimuth angle for the five lines of sight. The color lookup table at the bottom of the screen extends from -8 m/sec (blue) to +8 m/sec (red). Positive velocities are again defined as those away from the lidar. At an azimuth angle of 150, a near field telephone pole blocks the beam, eliminates aerosol returns, and results in poor velocity estimates. Over the 90° azimuth scan, the radial wind velocity shifts from values near +3 m/sec to values near -7 m/sec. From an azimuth angle of 90° to an azimuth angle of 135°, interesting small-scale (1 to 2 m/sec over ranges of 200 to 400 m) wind eddies are clearly present.

System Performance and SNR Model Validation

Performance model validation requires a large data base of well-documented field measurements. Two of the more important model inputs/assumptions are the system SNR and the degree (accuracy) to which the vector velocities can be inferred from radial velocity measurements. The degree to which the performance prediction models can be validated greatly impacts the prototype system design.

The validity of the lidar system SNR model relies heavily on how well atmospheric parameter dependencies at the operating wavelength are known both horizontally and vertically. The atmospheric parameters of interest are the volume backscatter coefficient, the atmospheric extinction coefficient, and the refractive turbulence structure coefficient. In addition, the system efficiency (photodetector quantum efficiency, optical efficiency, and heterodyne mixing efficiency) must be known fairly accurately.

Figure 4.1 Receiver power vs range

42

As a first step toward system SNR model validation, under a contract to Wright Laboratories, CTI recently completed field measurements of SNR versus range and elevation angle. The 2.09 mm, 21 mJ, 5 Hz, 10 cm aperture (8 cm e^{-2} intensity diameter) system was employed. The measured values of SNR were compared to those predicted by the model. Table 1 shows an example of the results. The skies were overcast during the measurements, so that refractive turbulence effects should be small (although no direct, quantitative measurement of refractive turbulence was made). For comparison purposes, model predictions for the standard refractive turbulence structure coefficient model (Hufnagel) are given in addition to this same model reduced by a factor of 0.01. As expected, the latter, 'weak' turbulence model predictions better match the measured values. The agreement is quite good for all elevation angles and all ranges.

Because the lidar system efficiency is currently not calibrated, Table 1 says nothing about the *absolute* value of the volume backscatter coefficient. Rather, it shows that the product of system efficiency and atmospheric backscatter (hb) matches well to that employed by the model (0.1 x $1x10^{-6}$ $m^{-1}sr^{-1}$ at ground level). More importantly, however, Table 1 shows that the parametric system dependencies (i.e., SNR versus altitude) are well-modeled by the simulation.

Receiver power versus range data taken between December and June 1992 has been used to produce Figure 4.1. This figure shows the time history of the maximum horizontal and vertical wind measurement ranges. We define the maximum measurement range as that range where the narrowband SNR drops to 0 dB (the average signal contribution to the detector output is equal to the average shot noise level). Through pulse averaging of three to four pulses to reduce noise speckle fluctuations, a narrowband SNR of 0 dB or more typically results in accurate velocity measurements.

For the horizontal data of Figure 4.1, the lidar beam was aimed north at an elevation angle of ~0.4° which allows the beam to pass just above the mountains to the north of Table Mountain. For the vertical data of Figure 4.1, the beam was aimed approximately straight up (elevation angle of 90°). For all the data, the transmitted beam was collimated and the transmitted pulse energy was roughly 20 mJ. The horizontal data comprises 73 irregularly spaced measurements (due, for example, to system shutdown for modifications and upgrades). The maximum horizontal measurement range fluctuates from 6 km to 30 km. Sixty-eight percent of the data is ≥ 15 km and 87% is ≥ 10 km. The vertical data represents the maximum measurement range obtained in the absence of clouds. No vertical data was taken when low-level clouds interfered with the measurement. The vertical data comprises 40 measurements that vary from 1.3 km to 9 km. Seventy-five percent of the data is ≥ 3 km and 87% is ≥ 2 km.

Since correlations in aerosol backscatter, atmospheric refractive turbulence, atmospheric transmission, and lidar system performance have not been made, the data is only intended to show the time history of the maximum measurement range for the ground-based 2 mm system in Boulder, CO. Variations in atmospheric refractive turbulence and aerosol backscatter can cause large fluctuations in SNR and probably large contributors to the observed measurement range fluctuations.

43

5.0 LASER TECHNOLOGY CONSIDERATIONS

5.1 BACKGROUND

CTI has led the development of efficient diode-laser pumped 2 micron lasers based around TM-doped YAG. Figure 5.1 shows data from a relatively early experiment. Here pulse energy is plotted against pulse spacing, i.e., the inverse PRF. Using only 6 W of pump power, this diode-pumped laser produced 4.5 mJ at 100 Hz, and 3 mJ at 200 Hz. Later improvements yielded > 5 mJ near 100 Hz and 4.2 mJ at 200 Hz. As shown in Section 2 these characteristics are close to those needed for a coherent lidar turbulence probe for the atmospheric boundary layer.

One of the prime areas of commercial interest for lidar systems is for airborne windshear detection. Based upon the laser results discussed above, CTI is presently collaborating with a major aerospace company to develop a flightworthy windshear detector. At present this transceiver is scheduled for delivery in April 1993.

Figure 5.2 shows a sketch of the transceiver as it is being developed . It consists of two lasers, the master oscillator (MO) and the slave oscillator SO). The MO power is split into several signals using optical fibers/couplers. Part of the MO signal is injected into the SO which forces this Q-switched laser to oscillate in a single longitudinal mode. The SO output is sent through the transmit/receive (T/R) switch out through a telescope and scanner. Radiation is collected with the same aperture, and is coupled into an optical fiber, and mixed with another port of the MO power. That signal is detected by a photodetector (PD1), which is connected to the signal processor. To ensure minimum uncertainty in the velocity estimates, a second detector (PD2) is used to monitor, on a pulse-to-pulse basis, the exact frequency shift between MO and SO.

In parallel with the hardware development, CTI is also working towards increasing laser pulse energies. We are presently able to achieve very high brightness from optical fibers pumped with the output from several separate diodes. Fiber pumping allows one to separate the pump optics from the laser rod. Using three diodes coupled into a single 200 micron diameter fiber, and a fourth diode coupling directly into the laser rod, we have achieved CW output powers exceeding 2 W. Much higher values are expected shortly, and Q-switched energy increases of almost a factor of two are also expected. For further increases in energy, more pump diodes can relatively easily be added. It is also important to note that 2 micron lasers, such as Tm:YAG, are tunable over quite large ranges. The CTI MO laser has been continuously tuned from about 2007 nm to 2023 nm (corresponding to > 1 THz), and the SO has been injection-seeded to 2021 nm. Since the emission peak occurs at about 2012 nm, this represents a detuning of 9 nm. The great tuning range, presently limited by the tuning etalons in the MO, is important since it enables one to select an optimal operating wavelength quite freely.

5.2 LASER TECHNOLOGY FOR DIAL MEASUREMENTS

DIAL meaurements of the type discussed above require a high prf source (typically 300 Hz) that can be switched between an absorbing (A) and non-absorbing (N) wavelength.
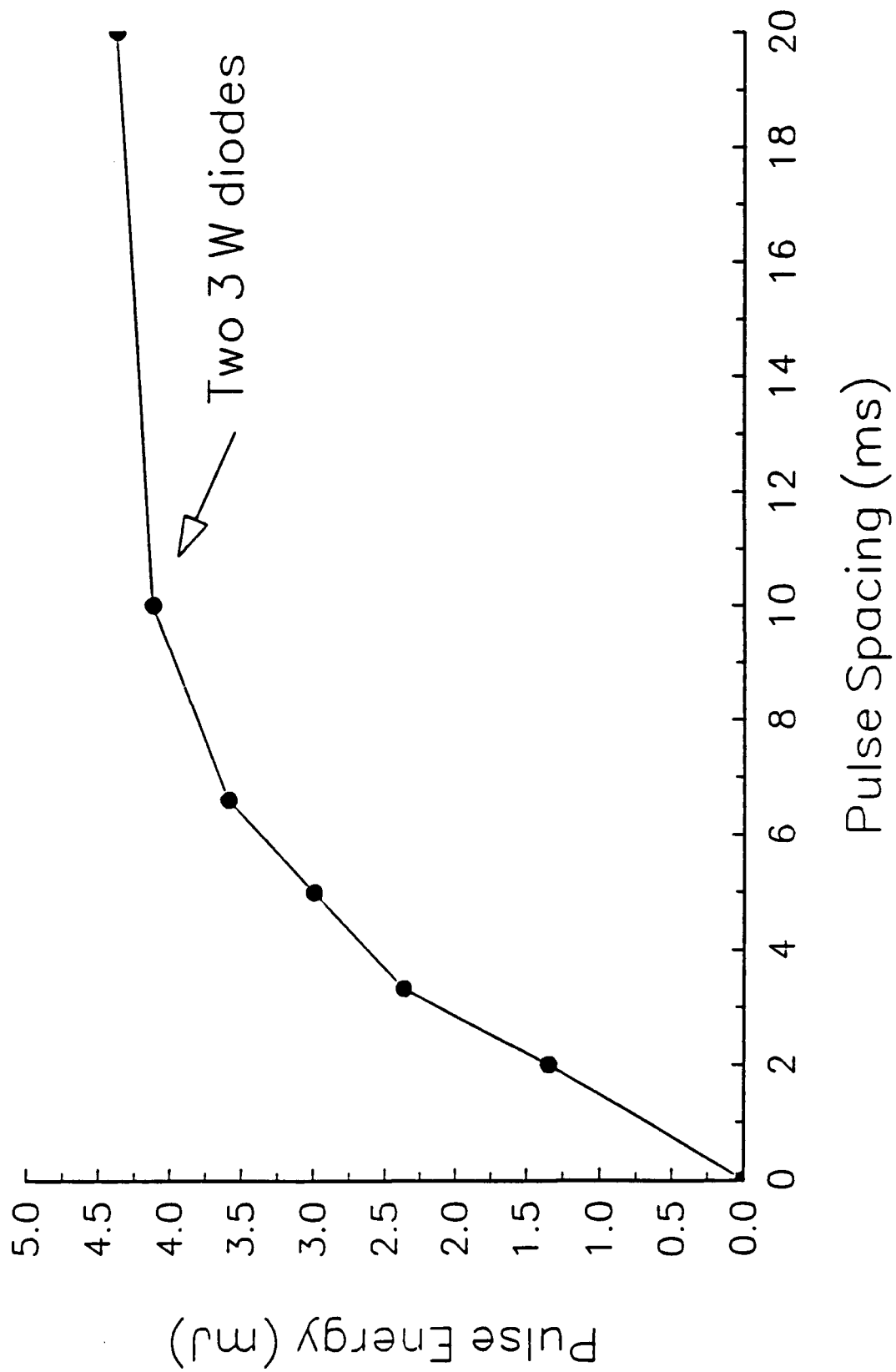
Figure 5.1. Pulse energy vs pulse separation for different pump modes.

Block Diagram of Coherent Laser Radar System
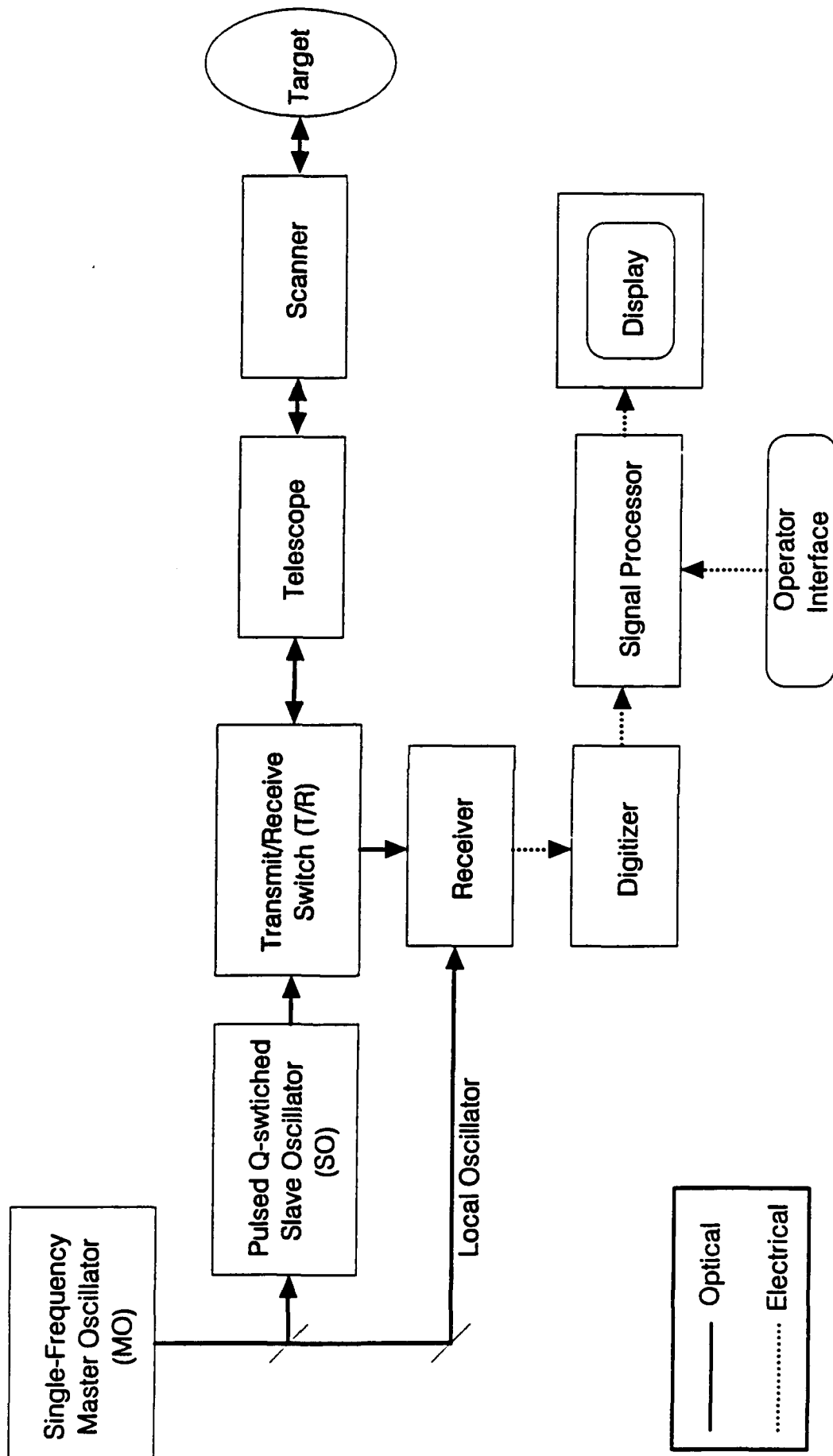
Coherent Technologies, Inc.

Figure 5.2. Windshear Transceiver Unit Diagram

Wavelength switching can be achieved in two basic ways. Either one source is used to tune between the A an N wavelengths, or two lasers are used, and the transmitter is switched between lasers. The first option is the more elegant, but also has some potential porblems that require fundamental studies. The main difficulty is not necessarily achieving rapid tuning. Rather it relates to ensuring that the laser wavelength settles down to the desired ones quickly, that repeatability is high, and that the laser always remains single-frequency. The second option is more straightforward, since two separate lasers can be stabilized quite well in wavelength.

We propose that the simplest and most cost-effective system is a hybrid one. Two CW master oscillators, stabilized to different wavelengths, are used to injection-seed a single slave oscillator. The main advantage of this approach is that only one slave oscillator is needed, which saves considerable cost and ensures that the energies transmitted at the two wavelengths are the same. The output energy of an injection-seeded laser is independent of the seed power, so small power differences between the two master oscillators are not important.

Wavelength Choices

In selecting suitable wavelengths for DIAL measurements, several issues must be considered. First, the non-absorbing one should have quite a low attenuation over the desired range. Second, the absorbing one should have an attenuation that is not too weak, but also not too strong. If it is weak, the differential absorption becomes more difficult, while if it is too strong, there may not be enough signal from the farthest desired range. The A wavelength must also be directly associated with water absorption, and should ideally not be contaminated by absorption due to other species. Figure 1.4a shows the MLS attenuation spectrum in the region of tuning of Tm:YAG lasers. There is a clear CO_2 overtone band covering much of the region, as well as other peaks associated with water and NO_2. Figure 1.4b shows the water spectrum alone. Several of the water lines overlap directly with CO_2 lines and are therefore unsuitable for this application. There are also several lines that do not overlap, notably the one marked with an arrow and the letter A at 2016.974 nm (vacuum wavelength - the air wavelength will be approximately 0.5 nm shorter). Detailed examination of that line shows an extinction coefficient of 3.389 km (29 dB/km roundtrip), and that the full width at the 95% peak value is approximately 0.019 nm, corresponding to 1.41 Hz. The width is important, as it directly relates to how frequency-stable the laser source must be. Further examination of the peak shows that neighboring CO_2 lines contribute < 3% of the total attenuation. This line is therefore an excellent choice for short-range water vapor measurements.

For the non-absorbing wavelength, the best choices is to operate at 2017.713 nm. The valley shows an adsorption of 0.1 per km at that point (0.4 db roundtrip attenuation per km). The width of the valley floor is approximately 0.078 nm, corresponding to a frequency width of 5.8 GHz.

Both of these wavelengths are easily accessible with an injection-seeded Tm:YAG laser. Continous tuning from 2006 to 2023 nm has been demonstrated.

Wavelength Stabilization

Stabilization of the two master oscillators (referred to as MO-N and MO-A) can be done relatively simply. In CTI's master oscillator design, two intracavity etalons are used to control the emission wavelength. Tuning is accomplished by rotating the etalons or varying their temperatures. The thin etalon determines the emission wavelength, while the thick one ensures that the laser operates in a single transverse mode. The mode spacing is determined by the free spectral range of the laser cavity, approximately 1.5 GHz in our case. The thick etalon is the element most sensitive to temperature variations, since it temperature tunes at a rate of approximately 1.4 GHz per degree C. Our lasers have the thick etalon stabilized to 0.1 degrees C, which ensures that the wavelength drift is no more than about 140 MHz. This has experimentally been determined to be sufficient to keep the laser from oscillating on more than one longitudinal mode. Note that preventing simultaneous oscillation at several frequencies is the real reason for keeping the laser temperature stabilized. Atmospheric features are typically broad compared with 140 MHz, and hence absolute wavelength accuracy to that level is not required.

Given these parameters, operation at a particular wavelength is really a question of settability. Once the oscillating wavelength has been set, simple temperature control of the laser will keep it at the right wavelength. Note here that the absolute wavelength stability requirement is 1.4 GHz for the A wavelength, and almost 6 GHz for the N wavelength. The only real difficulty is in setting the wavelengths to their proper values from the outset. A good monochromator can be used to set the wavelength to will below 1 nm, which is about one order of magnitude away from the desired accuracy. One way of getting to the 0.019 nm level is to use a wavemeter. A second method is simply to tune the laser(s) and look for maximum (N) and minimum (A) signals. This is probably a more accurate method, since it directly probes the absorption features we are interested in measuring.

While we do not anticipate difficulties in setting the laser wavelengths properly, we also note that there are active methods available for ensuring frequency stability. To do this one can build a water vapor absorption cell, through which the MO-A beam is passed. With a sufficient water vapor concentration and a long enough path, the transmitted power will vary dramatically as the laser wavelength is tuned through the absorption resonances. We estimate that a 1 m long cell maintained at 40 degrees C, and saturated with water vapor, through which the beam makes a single pass, will show a 12 % change in absorption at the peak, compared to off the peak. Such a cell is straightforward to construct, and furthermore, by letting the beam make multiple passes, or increasing the cell temperature, will increase the attenuation more.

The idea is then to measure the cell transmission and use a servo to lock onto the water resonance. Since drifts of the MO wavelength are expected to be small over several second timeframes, one of the MO etalons can simply be temperature tuned to close the servo loop. It is also possible with this active stabilization scheme to move off the absorbing peak in a controllable manner, so that the measurement range can be increased.

Switching between the two MOs can be achieved most simply by using a mechanical chopper, which can also be used to trigger the slave oscillator Q-switch. For example,
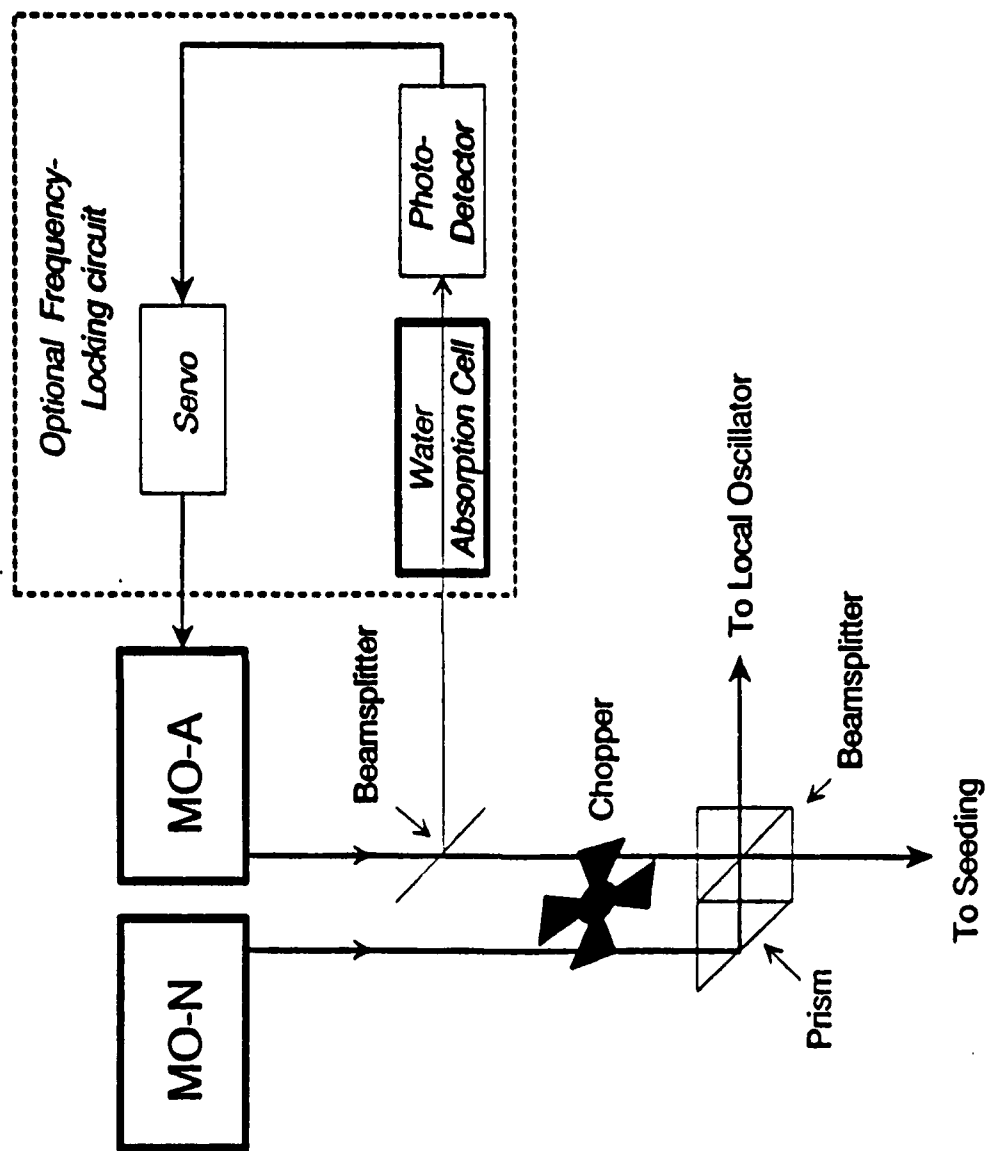
Figure 5.3 Frequency-Switched DIAL Transmitter

a 10-slot chopper wheel running at 15 rps, together with a prism/beamsplitter can be used to gate either of the two MO beams. With a simple LED/detector pair mounted to the chopper, low and high transitions can be used to trigger the Q-switch to fire. The optical assembly also has two output ports, so that one port can be used to seed the slave oscillator, while the other one is used to provide a local oscillator signal. Figure 5.3 shows a sketch of how such a dual-MO laser would be configured.

6.0 PROTOTYPE MEASUREMENT SYSTEM: CONCEPTUAL DESCRIPTION

A program to develop a lidar boundary layer probe as described in this report would have the following ingredients:

- construction or acquisition of a 1 or 2 watt mean power, pulsed diode pumped laser that can operate at several hundred Hz.

- incorporation of this lidar into a mobile scanning system

- development or acquisition of the 3D hydrodynamic model

- extension of the Kalman filter software to 3D

- verification of the vector wind retrieval process using LES output to simulate radial wind data for realistic boundary layer wind fields

- construction of the DIAL multiple wavelength switching capability

- acquisition of 3D radial wind data at a suitably instrumented location (airport)

- demonstration of vector wind retrieval

- acquistion of simultaneous 3D wind and DIAL data at an instrumented location

- demonstration and verification of water vapor retrieval

Under a Wright Laboratory contract, CTI is currently installing a 2 micron coherent laser radar transceiver into a compact, mobile van. The lidar van is shown in Figure 6.1. The lidar van includes a computer-controlled, super-hemispherical scanner that is fully integrated into the signal processing system. The lidar van is temperature controlled to operate in all environments.

The proposed diode-pumped 2.0 micron coherent laser radar measurement system will be smaller than the existing 2.1 micron system and could be easily installed on the lidar van optical bench. Because the lidar system is mobile, boundary layer measurements could be made in a variety of geographic locations.
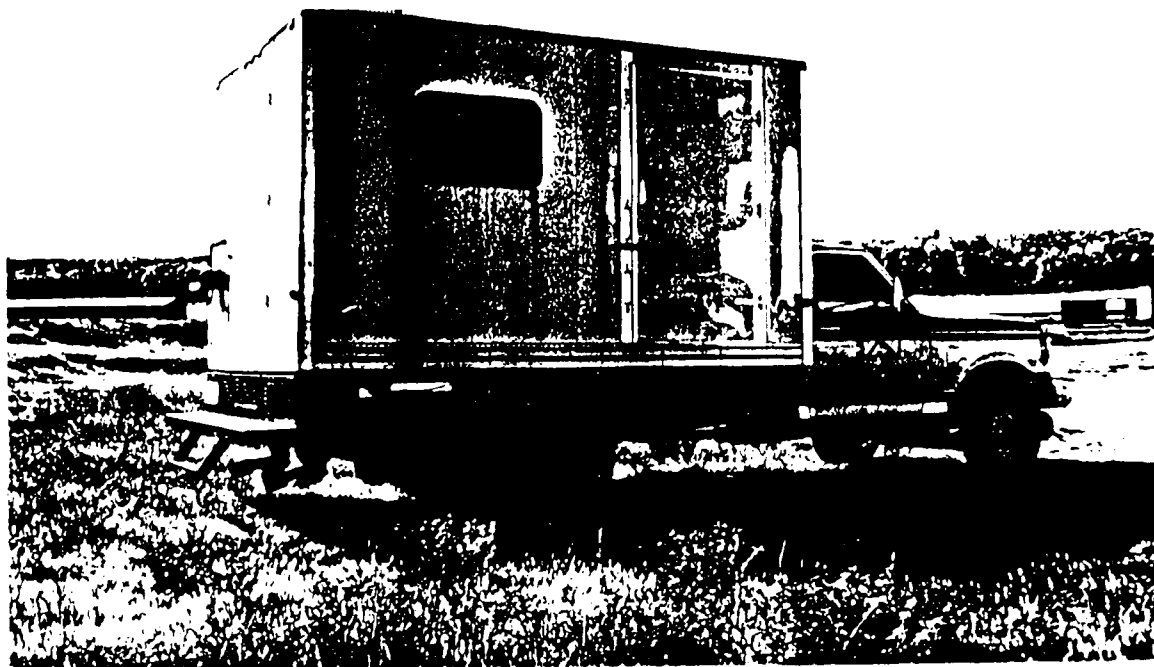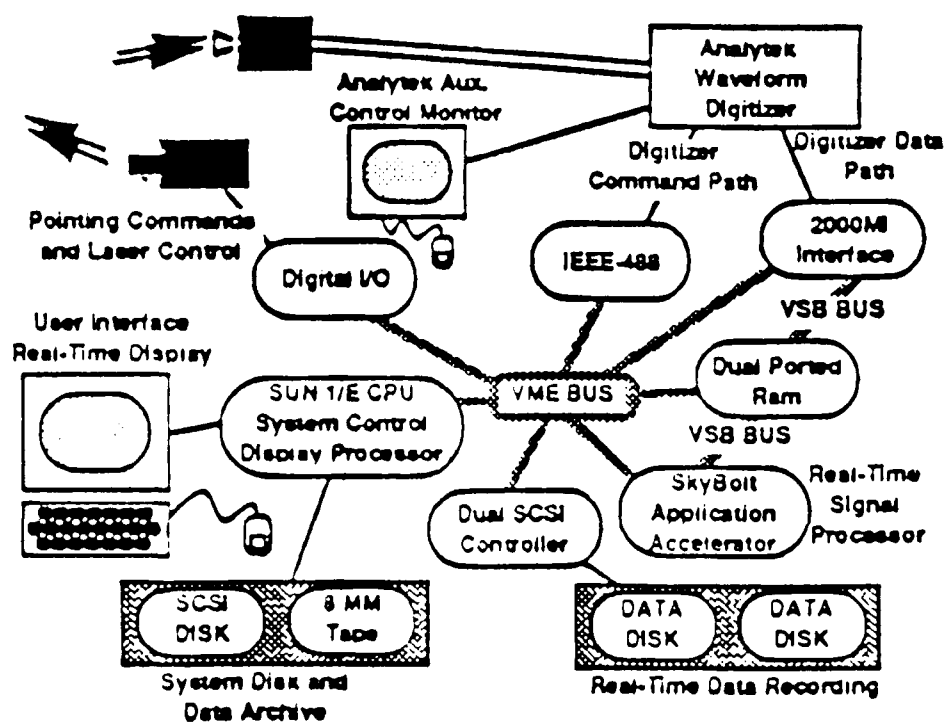
Figure 6.1 Wright Laboratory/CTI Lidar Van

Figure 6.2 The Real Time Lidar Processor

Real Time Lidar Processor (RTLP)

The Real Time Lidar Processor is a very flexible, completely programmable, data acquisition and analysis workstation. A system block diagram is shown in Figure 6.2. The system uses an Analytek waveform sampler for data acquisition, SkyBolt i860 applications accelerators for signal processing, a SUN SPARCstation for user interface and display, and other standard VME modules for scanner control and recording. The Analytek sample module uses a patented, VLSI analog storage module for burst acquisition and can operate at programmable rates of 1 MHz to 500 MHz, in 1 MHz steps with 12 bit accuracy. The module can be operated in either single (2 GHz maximum sampling rate) or dual (1 GHz maximum sampling rate) channel modes. The high-speed SkyBolt DSP is an application accelerator based on a 40 MHz i860 capable of 80 MFLOPS of peak performance, and an i960 processor to manage memory and I/O. The SkyBolt can be programmed in either FORTRAN or C, and is supported with a vast library of vector calls capable of performing at or better than 50% of the peak theoretical performance.

The RTLP performs real-time A-scope and range-resolved periodogram (spectral) processing of aerosol data. The fully integrated system provides processing, display, recording, and playback capabilities with real-time, color-coded graphics. The RTLP is fully programmable with standard outputs including plan position indicator (PPI) displays, color-coded range height indicator (RHI) displays, radial velocity mean and width versus range plots, and velocity versus height plots resulting from velocity azimuth (VAD) scans.

The RTLP can be easily upgraded to incorporate the requisite software for combined 3-D wind velocity and water vapor measurement computations. Due to the intense computational loads expected, completely real time operation may not be possible. For example, 100 MFLOPS of sustained performance may be required. In such circumstances, the RTLP would collect data for a period of 10 to 15 minutes, process data and output results for 40 to 50 minutes, process more data for 10 to 15 minutes, process data and output results for 40 to 50 minutes, and so on.

APPENDIX

[This appendix is extracted from CTI-TR-9207 report currently in preparation.]

Bayesian Data Assimilation

Given a set of measured data taken at periodic intervals over some specified spatial mesh in the atmosphere, the tast of a Kalman filter is to integrate these data with a known or modeled description of the expected dynamics to produce a 'best' estimate of the current atmospheric state.

In the present description the known atmospheric dynamics are specified by a set of equations of motion describing the constraints of continuity, energy and momentum conservation. For the planetary boundary layer the flow is well modeled as incompressible. The equation for this condition constitutes the continuity constraint. In general both a momentum and an energy constraint are also needed to describe the dynamics of a 3 dimensional boundary layer. In the analysis presented here we will consider only a neutrally stable atmosphere and will not include effects of latent heat release and other effects of buoyancy. In this limit only the momentum and continuity equations are needed to describe the flow. Expressing the velocity as the curl of a stream function automatically satisfies the continuity equation. The distribution and evolution of the source of this stream function (the vorticity) in space represents the fundamental description of the atmospheric state.

In general, each component of the vorticity vector forms the source function for a Poisson equation for the corresponding component of the velocity stream function

$$\nabla^2 \Psi = \Omega \tag{1}$$

The fluid velocity is the curl of the solution of this equation

$$\mathbf{U} = \nabla \times \Psi \tag{2}$$

By its definition this velocity field is incompressible. Given this prescription for calculating the velocity from the vorticity, the momentum equation for the vorticity describes the temporal evolution of the hydrodynamic state:

$$\frac{\partial \Omega}{\partial t} = -\mathbf{U} \bullet \nabla \Omega - \Omega \bullet \nabla \mathbf{U} + v \nabla^2 \Omega \tag{3}$$

The first two terms on the right hand side of Eq.(3) characterize the inherent dynamics of the modeled inviscid atmosphere. They represent respectively advective transport of vorticity and stretching of vorticity. The last term represents viscous diffusion. In most of the present analyses we will set this term to zero.

In the Kalman filter approach to data assimilation we need two models : one for the dynamics of the system being analysed and one characterizing the relationship between this dynamical model and the measured data. The Kalman filter merges these two models and generates a single equation describing the evolution of a best estimate of the system state.

We have chosen vorticity as the fundamental state variable. The evolution of the vorticity distribution can be represented in either of two modes: Eulerian or Lagrangian. In the Eulerian mode the state variable is the 3D vector vorticity evaluated at the nodes of a prespecified 3D spatial grid. In the Lagrangian mode discrete vortex elements are tracked as they move through space with the flow. Here the state variable has six component values for each vortex element: 3 vector components of circulation plus 3 position components.

In the next section the Kalman filter formalism will be developed for the Eulerian mode and in the following section for the Lagrangian mode. In both cases the filter has the basic form

$$\frac{d\mathbf{X}}{dt} = F(\mathbf{X}) + \int P(\mathbf{X},\mathbf{X}')\frac{\partial H(\mathbf{S},\mathbf{X}')}{\partial \mathbf{X}'}\{Z(\mathbf{S}) - H(\mathbf{S},\{\mathbf{X}\})\}d\mathbf{S}d\mathbf{X}' \tag{4}$$

Here $\mathbf{X}$ is the estimate of the state variable, $F(\mathbf{X})$ the (known or expected) state dynamics, $Z(\mathbf{S})$ the measured data at the data space point $\mathbf{S}$, $H(\mathbf{S},\mathbf{X})$ the prediction of the data at $\mathbf{S}$ for the state variable set $\{\mathbf{X}\}$, and $P(\mathbf{X},\mathbf{X}')$ is the expected covariance of the estimate $\mathbf{X}$. $P(\mathbf{X},\mathbf{X}')$ is to be calculated from an ancillary equation (the 'correct' Kalman filter) or is estimated empirically(sub-optimal filtering). In the form of Eq.(4) we have assumed uncorrelated, unit variance, white Gaussian noise for the measurement. In this form Eq. (4) may be thought of as being the result of a least squares fit of the data model to the measurements.

EULERIAN MODE - Tracking vorticity

For uncorrelated measurement noise having unit variance, the basic Kalman filter for the evolution of the estimate of the vorticity state of an inviscid fluid has the general form

$$\frac{\partial \hat{\Omega}}{\partial t} = -\mathbf{U}\bullet\nabla\hat{\Omega} - \hat{\Omega}\bullet\nabla\mathbf{U} + \int d\mathbf{x}'' P(\mathbf{x},\mathbf{x}'')\sum_\theta \int d\mathbf{x}' H(\mathbf{x}',\mathbf{x}'',\theta)\left[Z(\mathbf{x}',\theta) - Z_{pred}(\mathbf{x}',\theta;\hat{\Omega})\right]$$

$$\tag{5}$$

Here Z_{pred} is the current predicted value of the data measurement vector based on the current

estimate of the vorticity density field $\hat{\Omega}(\mathbf{x})$.

$$Z_{pred}(\mathbf{x}';\hat{\Omega},\theta_i) = \int H(\mathbf{x}',\mathbf{x}''',\theta_i)\hat{\Omega}(\mathbf{x}''')d\mathbf{x}''' \tag{6}$$

where q_i is the inclination of the ith line of sight;

The last term in Eq.(5) is the update correction to the predicted fluid dynamics that the Kalman filter prescribes to account for deviations between the actual observations and the current predictions.

For the purpose of demonstrating the use of the Kalman filter for the assimilation of lidar measurements with hydrodynamic models, we have limited the calculations presented in this note to a two dimensional atmosphere having only height and a single horizontal coordinate. However, for an actual implementation with real atmospheric data a full 3D model will be needed. Thus three dimensions will be retained in the formulation but the numerical examples are two dimensional. The extension to three dimensions is straightforward numerically although the implementation requires substantially greater computer resources.

Generally speaking, two dimensional turbulent flows behave qualitatively differently from three dimensional flows. The stretching term in the momentum equation (the second term on the right hand side of Eq. (5)) allows vorticity to be compressed and is responsible for the characteristic one-sided cascade of turbulent energy from large to small scales that typifies fully developed turbulence. In two dimensions, density of vorticity is conserved and the long term turbulent transport cascade processes differ. However, many of the basic short term structural characteristics of the turbulence process are qualitatively similar to those in 3D flows.

The Measurement Transfer Function H(x',x", q_i)

The measurement function relates the measured data to the function describing the atmospheric state. Since we have selected vorticity as the fundamental state variable and radial velocity along selected lines of sight for the measurement, the transfer function H includes the process of solving the Poisson equation to get the stream function, taking its curl to get velocity, forming the projection dot product to get the radial component, masking the 2D continuous distribution to limit the prediction to include just the sampled lines of sight, and finally, applying the range response function of the lidar. The first three of these steps as well as the last are homogeneous operations and can be represented as spatial convolution operations. The fourth is equivalent to multiplying by a spatial mask. Thus it is convenient to write H(x',x") in the form of a product of two single variable functions; a homogeneous term H_0 dependent only on the vector displacement between the two space points and a space local term H_1:

$$H(\mathbf{x'},\mathbf{x''}) = H_o(\mathbf{x'} - \mathbf{x''})H_1(\mathbf{x'}) \tag{7}$$

The first term is derived from the definition of the radial velocity

$$Z_{pred}(\mathbf{x};l) = \hat{\mathbf{n}}(l) \cdot \nabla \times \Psi(\mathbf{x}) \tag{8}$$

where $\hat{\mathbf{n}}(l)$ is the unit vector defining the lth lidar line of sight.

As will become evident, we will invoke a spatially homogeneous constraint to limit the complexity of the analysis. For such systems, many of the integral relations are most easily evaluated in the spatial Fourier domain. In anticipation of this we provide here various Fourier domain forms of the above expressions.

The Fourier transform of Eq. (8)

$$Z_{pred}(\mathbf{k};l) = \mathbf{H}_{\bullet}(\mathbf{k};l) \cdot \Omega(\mathbf{k}) = -i\left\{ \hat{\mathbf{n}}(l) \cdot \mathbf{k}/|\mathbf{k}|^2 \right\} \times \Omega(\mathbf{k}) \tag{9}$$

Interchanging the dot and cross operation allows us to identify the measurement transfer function as

$$\mathbf{H}_{\bullet}(\mathbf{k};l) = -i\,\hat{\mathbf{n}}(l) \times \mathbf{k}/|\mathbf{k}|^2 \tag{10}$$

For narrow beam lidar sampling, the second term in Eq. (7) is a delta function defining the locations sampled by the lidar beam

$$H_1(\mathbf{x};l) = H_1(x,y,z;l) = \delta(z - x\cos(\varphi)\tan(\theta))\delta(z - y\sin(\varphi)\tan(\theta)) \qquad (11)$$

where q and j are the polar and aximuthal angles of the lth line of sight of the lidar.

The State Covariance term P(x',x")

The state covariance term in a Kalman filter is supposed to be evaluated from an ancillary differential equation that continually estimates and updates the precision and expected correlations of the predicted state estimates. In a true Kalman implementation this a non-linear Ricatti type equation for a two variable function, and can dominate the computational load when the number of state variable components is large. In most applications to the estimation of multidimensional scenes, the computational requirements for this evaluation are extreme and, as a result, sub optimal prescriptive models for P(x',x") are usually used. This is the approach we will adopt here. A similar approach is commonly used in weather forecasting where the weather estimates are generated using a procedure similar in principle to Eq. (5) with empirical prescriptions used for the influence function P(x',x"). These algorithms are often refered to as OI methods ('Optimal Interpolation') to distinguish them from true Bayesian or Kalman prescriptions in which a formally derived statistical algorithm is used to estimate P(x',x"). In this note we will use the generic term Kalman filter to refer to both forms of data analysis.

The term P(x',x") term is formally defined as the covariance of the error of the state estimate and can be expressed as

$$P(\mathbf{x'},\mathbf{x''}) = <(\Omega' - \hat{\Omega'})(\Omega'' - \hat{\Omega''})> \qquad (12)$$

where W' is the true vorticity at the point x', $\hat{\Omega'}$ its estimate, and the brackets <> mean expected value. When the vorticity is spatially uncorrelated and white, Eq. (5) reduces to a least square estimate (it actually becomes the maximum likelihood estimate: in Eq. (5) the measurement noise has been assumed white and uncorrelated so that the ML result is simply the least square value).

When the state estimates are all uncorrelated, each of the terms in Eq. (5) can be easily interpreted. Replacing P(x',x") by P_0 times the delta function and integrating gives

$$\frac{\partial \hat{\Omega}}{\partial t} = -\mathbf{U} \bullet \nabla \hat{\Omega} - \hat{\Omega} \bullet \nabla \mathbf{U} + P_o \sum_\theta \int d\mathbf{x'} H(\mathbf{x'},\mathbf{x},\theta) \left[Z(\mathbf{x'},\theta) - Z_{pred}(\mathbf{x'},\theta;\hat{\Omega}) \right] \quad (13)$$

The integral term in Eq.(13) can be recognized as proportional to the derivative of the error energy (integrated over all space) with respect to the vorticity estimate at the space point x':

$$\frac{\partial E}{\partial \hat{\Omega}} = -0.5 \frac{\partial}{\partial \hat{\Omega}} \sum_\theta \int d\mathbf{x'} \left[Z(\mathbf{x'},\theta) - Z_{pred}(\mathbf{x'},\theta;\hat{\Omega}) \right]^2 \qquad (14)$$

56

Thus the Bayesian estimation process embedded in the Kalman filter (Eq. 13) adjusts the current estimate of the vorticity state at each time step in two ways. First the estimate is advected and concentrated according to the normal fluid dynamic rules for vorticity dynamics of inviscid flow. Second the entire vorticity field is altered at each point in space according to one step of a steepest descent prescription whose goal is to minimize the current mean square discrepancy between the actual data and the current predictions.

This latter independent adjustment of the vorticity at each point in space is appropriate only when the individual vorticity values are truly independent. A finite $P(x',x'')$ function allows for correlation between neighboring points. The integration over x' in Eq (13) blurs out the connections between the data error terms and the individual vorticity state values and allows the vorticity correlations predicted dynamically to be maintained during the data update process.

In a suboptimal analysis we need to select an appropriate form for $P(x',x'')$. For a homogeneous boundary layer we can require that P be only a function of the (vector) horizontal difference distance $x'-x''$ together with a parametric dependence on the height. To simplify the 2D demonstration analysis we will assume initially a dependence on the 3D vector difference displacement. This will allow Fourier transform methods to be used to simplify the computation of the update of the vorticity state. In this limit P is described completely by its Fourier transform $P(k)$. In the present analysis we will assume simple, parametric forms for $P(k)$. In a more extended analysis it would be appropriate to develop more direct models that more accurately represent the full Kalman formalism.

LAGRANGIAN MODE - Tracking Vortices

Instead of treating the vorticity density as the fundamental state variable, we imagine a model of the fluid in which a cloud of preexistent discrete vortex elements are the source of the velocity field. In expectation the density of this cloud is the vorticity. However, the computation tracks individual vortex elements (their location, orientation, and strength). The velocity of any element can be calculated by directly summing the Green's function contribution from all other elements. Alternately it may be evaluated by adding up the contributions of all vortex elements in each mesh cell to get a vorticity density, solving a Poisson equation for the stream function throughout the mesh, and interpolating the value of the stream function curl at the vortex location to get the velocity. (Using fast Poisson solvers, the first method requires of order N^2 operations per time step where N is the number of vortex elements, whereas the second requires of order $N+M$ $\log(M)$ with M the number of mesh cells.)

Both Lagrangian and Eulerian methods are commonly used in computing three dimensional fluid flows and both have their advantages and disadvantages. For simply computing the flow of a fluid both methods remain relatively closely related in their computational implementations. However, in the Kalman filter assimilation of concurrent data, distinct differences arise that have conceptually different mathematical interpretations. These arise primarily from the manner in which the system state is defined. In the Eulerian approach, the three component vector vorticity is the natural state variable, and the filter has the formal form of an equation for 3D vector fluid evolving in 3D space under the influence of a distributed source function generated by local differences between measured and predicted data values. In the Lagrangian approach, the state variable is a six component vector (vortex element circulation and spatial location (both 3D vectors)) and the formal form of the Kalman filter is now a cloud of 6D vector elements evolving in a 6D space. This cloud has fluid-like qualities and the filter analysis can be recast formally into a fluid description in 6D state space. This space can have conceptually different properties than the 3D spatial space used in the Eulerian description.

The Lagrangian state variable, **X=(a,x)**, has six vector components for each vortex element; x is the position of the element and a its circulation. The flow field associated with the elementary vortex element located at x_p and having circulation a_p is described by its stream function:

$$\Psi = a_p f(\mathbf{x} - \mathbf{x}_p) \tag{15}$$

where f is the Green's function for a unit source at the origin:

$$f(\mathbf{x}) = 1 / |\mathbf{x}| \tag{16}$$

The fluid velocity u and its projection H on the the lidar line of sight are given by

$$\mathbf{u} = \nabla \times \Psi = \sum_p \mathbf{a}_p \times \nabla f(\mathbf{x} - \mathbf{x}_p)$$

$$\tag{17}$$

$$H(\mathbf{x}, \mathbf{x}_p, \mathbf{a}_p) = \mathbf{n} \cdot \mathbf{u} = \sum_p \mathbf{n} \cdot \mathbf{a}_p \times \nabla f(\mathbf{x} - \mathbf{x}_p) = \sum_p \mathbf{n} \times \mathbf{a}_p \cdot \nabla f(\mathbf{x} - \mathbf{x}_p)$$

The Lagrangian update equation for the Kalman filter is derived from Eq.(4). To simplify the analysis we will assume a particular form for the covariance P(**X,X'**), i.e.,

$$\text{P(\textbf{X,X'})=P((x,a),(x',a'))} = \begin{pmatrix} P(\mathbf{x} - \mathbf{x}') & 0 \\ 0 & \sigma_a^2 \delta(\mathbf{a} - \mathbf{a}') \end{pmatrix}. \tag{18}$$

The first assumption that P depends only on the separation in the 6D state space between the two points (x,a) and (x',a') is equivalent to assuming homogeneity (no preferred spatial origin, no preferred vortex orientation or strength and should be valid in homgeneous turbulence. In a boundary layer, however, the assumption fails for turbulence scales comparable to the local distance from the bounding surface).

The second assumption that the circulation estimates are delta function correlated is introduced without justification and is purely for convenience ⌐f ¹he initial analysis.

In this approximation the update equation for the vortex element positions becomes (from Eq. (4))

$$\frac{d\mathbf{x}_p}{dt} = F(\mathbf{x}_p, \mathbf{a}_p) + \int P(\mathbf{x}_p - \mathbf{x}') \frac{\partial H(\mathbf{s}, \mathbf{x}', \mathbf{a}_p)}{\partial \mathbf{x}'} \{Z(\mathbf{s}) - H(\mathbf{s}, \{X\})\} d\mathbf{s} d\mathbf{x}' \tag{19}$$

58

Because of the homogeneity assumption we can rewrite the data term in Eq(19) as the gradient of a psuedo potential evaluated at the location of the vortex:

$$\frac{d\mathbf{x}_p}{dt} = F(\mathbf{x}_p, \mathbf{a}_p) + \nabla V(\mathbf{x}, \mathbf{a})\big|_{\mathbf{x}=\mathbf{x}_p, \mathbf{a}=\mathbf{a}_p} \qquad (20)$$

where

$$V(\mathbf{x}, \mathbf{a}) = \int P(\mathbf{x} - \mathbf{x}') H(\mathbf{s}, \mathbf{x}', \mathbf{a})\{Z(\mathbf{s}) - H(\mathbf{s}, \{\mathbf{X}\})\} d\mathbf{s} d\mathbf{x}' \qquad (21)$$

Eqs. (20) and (21) demonstrate very clearly the basic mechanics of the Kalman filter when applied to distributed measurements that sparsely sample a continuous dynamical field. As a result of the basic Bayesian formulation we expect (i.e., we demanded) that the dynamical model and the data be combined to yield a 'best' estimate of the current state. This best estimate criterion is defined as being that which produces the minimum expected uncertainty of the estimated state (minimum variance in the present description because of the assumption of uncorrelated measurement noise in Eq. (4)). When the measured data disagree with current predictions Eq. (21) establishes an error signal at those locations of the disagreement. This error signal is multiplied by the expected value of the measurement to form an error source function. This latter multiplication is necessary so that finite measurement values originating from regions from where no measured levels are expected are properly interpreted as being noise and will be rejected. This source signal is then convolved with the state covariance model P to create a scalar potential field V. This latter convolution ensures that all state points in the vicinity of an error signal that are correlated will respond to the error. The gradient of this potential field estabishes an advection velocity field that will induce a motion designed to reduce the error signal. This velocity is added to the physical velocity field due to the interaction between all the currently estimated vortices.

The advantage of the convolution form for establishing the error advection field cannot be understated. A major problem in steepest descent relaxation methods (of which this in one) is the difficulty of getting the whole solution field to respond to highly localized errors without getting stuck in local minima. By having the error signals blurred out by the covariance function, it is possible to make all points in the field feel some influence of every error signal, local as well as distant, and thus allow all points to respond instantaneously and continuously. Because the response at a given vortex depends on the coordinates and strengths of all other vortices, a smooth type of response can be expected if the effective psuedo force field is suitably chosen.

In principle, the influence function P should be calculated from a separate covariance evolution equation. Without the homogeneity assumption to limit the functional dependence this can be a horrendously difficult task. For homogeneous environments, P is simply a scalar function of one space variable and should be easily computed (especially since it depends only on the expected data statistics, not the actual data itself). In the present analysis, however, we do not attempt to solve directly for P but will arbitrarily prescribe forms heuristically.

Substituting for H from Eq.(17) and setting F(x) equal to the local fluid velocity gives

$$\frac{d\mathbf{x}}{dt} = \mathbf{u}(\mathbf{x}) + \nabla \left[\int P(\mathbf{x} - \mathbf{x}') H(\mathbf{s}, \mathbf{x}')\{Z(\mathbf{s}) - H(\mathbf{s}, \{\mathbf{X}\})\} d\mathbf{s} d\mathbf{x}' \right] \qquad (22)$$

In Eq. (22) the integration over s is limited to the actual measured points. For any measurement system which simply samples points in the state space it is convenient to introduce a mask function $H_s(\mathbf{x}, \mathbf{n})$ to accomplish this constraint. Invoking also the homogeneous condition for H then gives

$$\frac{d\mathbf{x}}{dt} = \mathbf{u}(\mathbf{x}) + \nabla V(\mathbf{x}, \mathbf{a}) \tag{23}$$

where V is the scalar 'pseudo-potential' defined by

$$V(\mathbf{x},\mathbf{a}) = \int P(\mathbf{x}-\mathbf{x}') \sum_n \left[H(\mathbf{x_s}-\mathbf{x}') H_s(\mathbf{x_s},\mathbf{n}) \left\{ Z(\mathbf{x_s}) - \sum_q H(\mathbf{x_s}-\mathbf{x_q}) \right\} d\mathbf{x_s} \right] d\mathbf{x}' \tag{24}$$

where now the integrations over x' and $\mathbf{x_s}$ extend over the full state space. In recognition of the fact that H depends on the lidar look direction **n**, we have separated the contributions from separate look directions into a sum over these directions.

Equations 23 and 24 are convenient for numerical integrations using Fourier methods for evaluating the advection fields. Using the definitions for u and H

$$\mathbf{u}(\mathbf{x}_p) = \sum_p \mathbf{a_p} \times \nabla f(\mathbf{x}-\mathbf{x_p}) \tag{25}$$

$$H(\delta\mathbf{x},\mathbf{a},\mathbf{n}) = \mathbf{n}\cdot\mathbf{a} \times \nabla f(\delta\mathbf{x}) = \mathbf{n}\times\mathbf{a}\cdot\nabla f(\delta\mathbf{x})$$

we may write the psuedo-potential function in the form

$$V(\mathbf{x},\mathbf{a}) = \int P(\mathbf{x}-\mathbf{x}') \sum_n \left[\mathbf{n}\times\mathbf{a}\cdot\nabla f(\mathbf{x_s}-\mathbf{x}') Z_s(\mathbf{x_s},\mathbf{n}) \right] d\mathbf{x}' ds \tag{26}$$

where $Z_s(\mathbf{x},\mathbf{n})$ is the (masked) error source function for the line of sight n:

$$Z_s(\mathbf{x},\mathbf{n}) = H_s(\mathbf{x},\mathbf{n}) \left\{ Z(\mathbf{x}) - \sum_q H(\mathbf{x}-\mathbf{x_q},\mathbf{n},\mathbf{a_q}) \right\} \tag{27}$$

The Fourier transforms of H and of the true velocity fields are

$$H(\mathbf{k},\mathbf{n},\mathbf{a}) = i\mathbf{n}\times\mathbf{a}\cdot\mathbf{k}f(\mathbf{k}) \tag{28}$$

$$\mathbf{u}(\mathbf{k}) = i\sum_p \mathbf{a_p} \times \mathbf{k}f(\mathbf{k})\exp(i\mathbf{k}\cdot\mathbf{x_p})$$

The psuedo-potential may be written in the form

$$V(\mathbf{k},\mathbf{a}) = -iP(\mathbf{k})f(\mathbf{k})\mathbf{k}\cdot\mathbf{a}\times\mathbf{Z_s}(\mathbf{k}) / R\Delta s\Delta x\Delta t \tag{29}$$

where we have defined the masked measurement error vector $\mathbf{Z_s}(\mathbf{x})$ as a vector sum over all lines of sight

$$Z_s(x) = \sum_n nZ_s(x, n) \qquad (30)$$

This quantity is simply the 3D distribution of sensed error radial velocity (converted to radial vectors at each measurement point and set to zero at all other points).

Equation(29) can be rewritten in terms of the curl of this quantity, i.e., in terms of a measurement error vorticity field $\Omega_s(x) = \nabla \times Z_s(x)$:

$$V(k, a) = P(k)f(k)a \cdot \Omega_s(k) / R\Delta s\Delta x\Delta t \qquad (31)$$

Thus the scalar pseudo-potential V is equal to the projection of the vortex circulation vector on to a vector potential function quantity $A_s(x)$:

$$V(x, a) = a \cdot A_s(x) \qquad (32)$$

This vector potential function can be interpreted as being a vector field generated by the (vector) source function $\Psi_s(x)$ with the covariance function P(x) serving as the Green's function. In Fourier space

$$A_s(k) = P(k)\Psi_s(k) / R\Delta x\Delta s\Delta t. \qquad (33)$$

In turn the quantity $\Psi_s(x)$ is the stream function associated with the pseudo vorticity error field Ω_S which is derived from the observed line-of- sight velocities according to Eqs. 27 and 30:

$$\Psi_s(k) = f(k)\Omega_s(k) \qquad (34)$$

In other words

$$A_s(k) = P(k)f(k)\Omega_s(k) / R\Delta s\Delta x\Delta t \qquad (35)$$

Equations (23) to (34) provide a means for calculating the evolution of positions of the discrete vortex elements given the input data and the values of the vortex strengths.

Equations describing the evolution of the circulations of the vortex elements may be constructed using a similar analysis. From Eq. (4) and (18), and using the same assumptions used in deriving Eq. (22) to (30), we obtain an expression for the evolution of the estimates of the vortex element strengths:

$$\frac{da_p}{dt} = \int \sigma_a^2 \delta(a - a_p) \frac{\partial Z_p(x_p - x_s, a, n)}{\partial a} Z_s(x_s) dadx_s / R\Delta s\Delta t \qquad (36)$$

61

Eq (25) allows this equation to be rewritten in the form

$$\frac{d\mathbf{a}_p}{dt} = \sum_{\mathbf{n}} \mathbf{n} \times \int \sigma_a^2 \delta(\mathbf{a} - \mathbf{a}_p) \nabla f(\mathbf{x}_p - \mathbf{x}_s) Z_s(\mathbf{x}_s, \mathbf{n}) d\mathbf{x}_s d\mathbf{a} / R\Delta s \Delta t \qquad (37)$$

Expressed in the Fourier domain

$$\frac{d\mathbf{a}_p}{dt} = -i\sigma_a^2 \int \mathbf{k} \times \mathbf{Z}_s(\mathbf{k}) f(\mathbf{k}) \exp(i\mathbf{k} \cdot \mathbf{x}_p) d\mathbf{k} / R\Delta s \Delta t$$

$$= -\sigma_a^2 \int f(\mathbf{k}) \Omega_s(\mathbf{k}) \exp(i\mathbf{k} \cdot \mathbf{x}_p) d\mathbf{k} / R\Delta s \Delta t \qquad (38)$$

In other words, the growth rate of the strength of vortex element $\mathbf{p}$ is just proportional to the negative of the pseudo-stream function evaluated at the vortex location

$$\frac{d\mathbf{a}_p}{dt} = -\frac{\sigma_a^2 \Psi_s(\mathbf{x}_p)}{R\Delta S \Delta t} \qquad (39)$$